Robotics and Computer–Integrated Manufacturing 89 (2024) 102743

Contents lists available at ScienceDirect

Robotics and Computer-Integrated Manufacturing

journal homepage: www.elsevier.com/locate/rcim

Full length article

In-situ elastic calibration of robots: Minimally-invasive technology, cover-based pose search and aerospace case studies

Bruno Monsarrat [a,*], Julien-Mathieu Audet [a], Yves Fortin [a], Gabriel Côté [a], Michael Vistein [c], Lars Brandt [c], Ahmad Sadek [b], Florian Krebs [c]

[a] National Research Council Canada (NRC), Advanced Robotics and Mechatronic Systems (ARMS), Aerospace Manufacturing Technology Center (AMTC), 2107 Chem. de Polytechnique, Montréal, Québec, H3T 1J4, Canada
[b] NRC-AMTC, Hybrid Manufacturing, 2107 Chem. de Polytechnique, Montréal, Québec, H3T 1J4, Canada
[c] German Aerospace Center (DLR), Center for Lightweight Production Technology (ZLP), Am Technologiezentrum 4, 86159 Augsburg, Germany

ARTICLE INFO

Keywords:
In-situ elastic robot calibration
Cover-based pose search technique
Repeated cross-validation algorithm
Real-time path correction under load
Automated fiber placement (AFP)
Robotized machining

ABSTRACT

This paper presents a novel technology for the in-situ robot elastic calibration (IREC) in industrial settings. It was especially formulated for robots that are used for accuracy demanding processes involving an exchange of force between the robot and the processed part. The calibration method was developed to conciliate requirements of minimal invasiveness, for seamless deployment in industrial settings, together with a high degree of coherence with the spectrum of action of the robot in production. The method relies on the achievement of a set of controlled load cases exerted in tribologically resisted directions after the robot is engaged against a constraint in order to establish accurate force–displacement relationships. A minimal set of engagement poses is efficiently determined using a new pose search technique involving a metric cover-based approximation heuristics applied on the surface of the constraint. The calibration apparatus and method are presented through the lens of accuracy competency development charts (Codecs), the graphical outputs of a repeated cross-validation algorithm. This new monitoring tool allows visualizing how the accuracy of deviation under load prediction grows during the calibration as a function of the number and distribution of calibration poses, and how this growth is influenced by the complexity of the load cases and that of the elastic model. Two case studies are presented to highlight both the efficiency and generality of the proposed method and algorithms, first the robotized automated fiber placement (AFP) processing of a 3D thermoplastic aerostructure and subsequently the robotized machining of a representative primary aluminium aerospace part. In these applications, the mean deviations were reduced respectively by 89.30 % and 83.08 %, allowing the achievement of the desired process tolerances.

1. Introduction

According to recently published analytics, the aerospace robotics segment is projected to grow at a significant compound annual growth rate of 11.4% until 2026, as an answer to the projected post-pandemic increase in global aircraft demand and growing shortage in the workforce capable of performing specialized manual operations such as component drilling, fastener installation or part finishing [1]. These robotic technological platforms industrialized in the aerospace industry, typically in high value-added operations, offer a means to reduce production costs, improve quality and increase throughput during the manufacturing of both fixed- and rotary-wing aircrafts [2].

This deployment of industrial robots in the aerospace sector, however, is subject to stringent requirements in terms of process accuracy tolerances, process control and traceability in robotic systems used for the manufacturing and assembly of aerostructures. The first requirement poses a particularly significant challenge due to the greater actuator and structural elasticities in traditional polyarticulated industrial robots compared to highly rigid gantry-type motion platforms. In the case of the robotization of drilling operations for instance – a modern commercial aircraft requiring millions of accurately-drilled holes – the industrial robot typically needs to first achieve a clamp-up against the aerostructure, at an amplitude of at least of few hectonewtons in order to close the gap between the components to be assembled. While the robot accuracy just before clamp-up has been shown to be effectively managed using a variety of approaches (see for instance [3–5]), the deformation of the robot under the clamp-up load induces both a loss of normality and a slippage phenomenon between the end-effector and the exterior skin of the component, causing unacceptable marks

* Corresponding author.
E-mail address: bruno.monsarrat@cnrc-nrc.gc.ca (B. Monsarrat).

https://doi.org/10.1016/j.rcim.2024.102743
Received 15 September 2023; Received in revised form 14 December 2023; Accepted 24 February 2024
Available online 16 March 2024

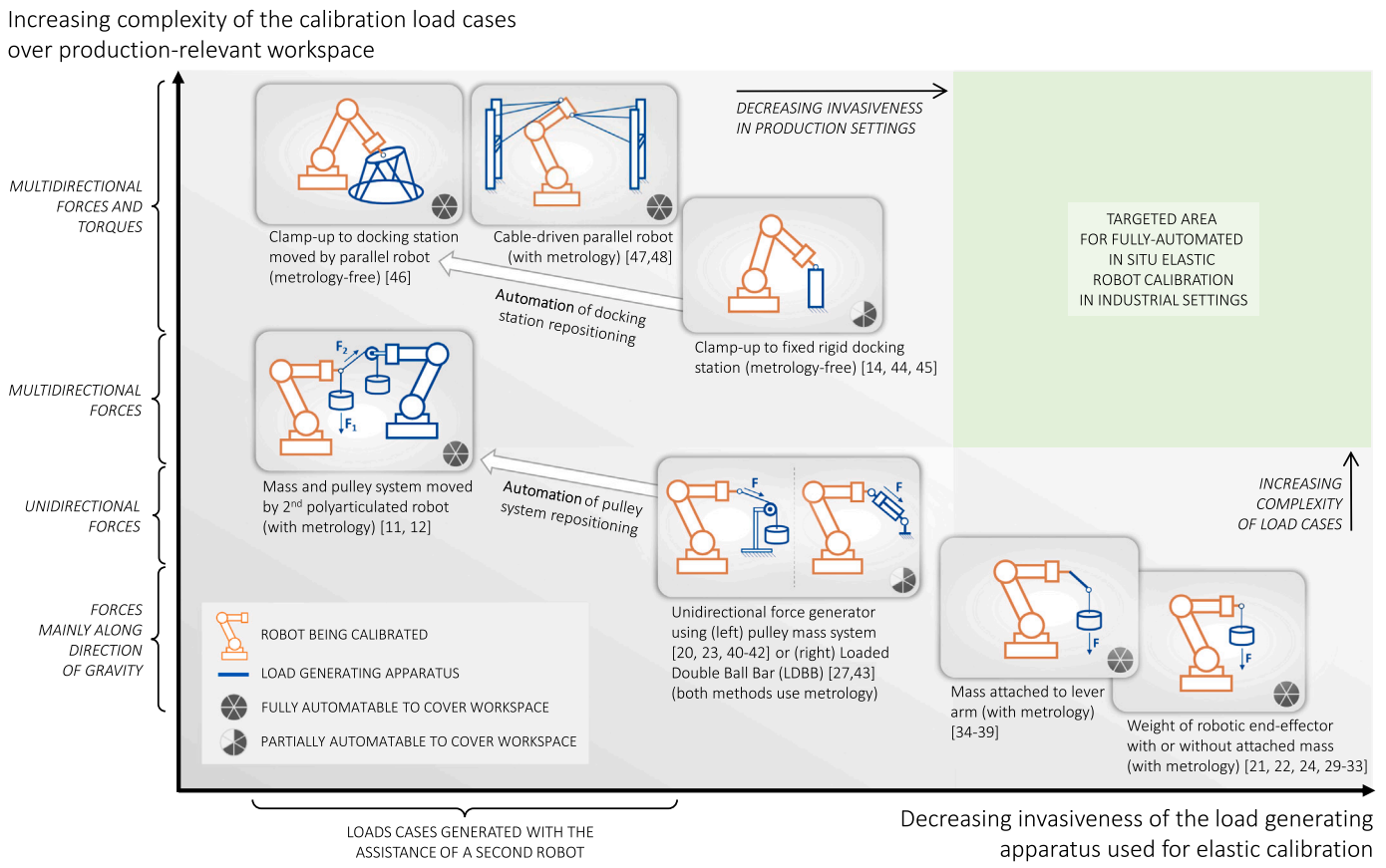

Fig. 1. Schematic illustration of the authors' perspective on the distribution of methods proposed in the art for elastic robot calibration according to the complexity of the load cases that can be generated, correlated with their invasiveness and ease of in-situ use in the production environment. For each method, the level of automation that can be achieved is considered as a third metrics (pie chart). The green area highlights the gap identified by the authors, where a conciliation is achieved between requirements of low invasiveness and those of coherence of the calibration load cases with the spectrum of action of the robot.

and out-of-tolerance holes. Many industrial robots exploited today on the assembly lines of aeronautic OEMs worldwide have benefited of an invention that has represented a major breakthrough to efficiently mitigate these phenomena, making use of an instrumented passive 4-degree-of-freedom dislocation mechanism located immediately behind the clamp-up nose. This device is activated just before the clamp-up load is increased to allow freeing the robot deformation along 4 axes, then measuring these offsets and correcting the robot pose accordingly [6,7].

Contrary to the aforementioned case of discrete processes such as drilling, where an internal dislocation of the end-effector followed by a Cartesian correction of the deformation is possible, continuous path processes used in the aerospace industry, such as automated fiber placement, machining or friction stir welding, induce Cartesian deviations at the robot tool-center-point (TCP) that evolve dynamically as a function of the changing robot posture and interaction forces between the tool and the part being processed. For such applications, several works have illustrated in recent years the strong potential of model-based path compensation methods for robot accuracy improvement, in which deviations caused by process forces are compensated for via offline [8–20], or inline [21–27] path compensation techniques, or a combination of both methods [28].

As it has been very well highlighted in several of the aforementioned works, the level of fidelity between the elastic model and the physical structural signature of the robot is a key enabling pillar in the growth of the accuracy under load during an elastic calibration process. Beyond the aspect of the fidelity of the modeling approach, a factor that has been less explored in the art is the degree of coherence of the elastic parameter identification protocol with the spectrum of action of the robot in its industrial environment. The notion of *spectrum of action* refers here to the set of planned operations of the robot in production from a perspective of both its application-relevant workspace and range of process-induced sollicitations. As the authors highlight in Section 4 of the present paper, the accuracy competency development of the robot under load is highly sensitive to that degree of coherence. In other words, achieving a maximal degree of coherence between the identification protocol and the spectrum of action of the robot in production, from the perspective of both the calibration poses and the calibration load cases, is shown to constitute a key technological foundation in order to enable the highest possible accuracy of the robot operating under process loads.

Through consultations with North-American and European aerospace industrial stakeholders, a strong consensus was expressed vis-à-vis the need for *in-situ*, *minimally-invasive* and *fully-automated* robot calibration methods that could be deployed directly in industrial settings in presence of the hardware used during full-rate production activities. Beyond the initial launch in production, such methods shall also be easily usable for system recertification by the maintenance personal during production shutdown periods that typically occur on an annual or biennial basis.

In view of these requirements, we have conducted a review of the methods proposed in the art through the lens of their degree of coherence with the robot spectrum of action, expected to operate under multidirectional process loads, correlated with their degree of invasiveness and ease of in-situ deployment in production environments. This distribution of existing methods is schematically illustrated in Fig. 1, where methods best conciliating these requirements would be positioned in the green area. More specifically, existing methods can be classified under 5 major categories.

Category 1: Refs. [21,22,24,29–33] all have in common the presentation of elastic robot calibration methods where the applied load cases are acting along the direction of gravity. While some work rely solely on the self-weight of the arm with its mounted end-effector (spindle, gripper, etc.) [31,33], several works proposed the use of an additional mass attached or suspended in the vicinity of the end-effector tool-center-point (TCP), combined with metrology measurements [21,22,24,29,30,32]. Such methods have a low invasiveness and allow for in-situ fully-automated robot calibrations using coordinated metrology measurements. The fact that the external wrench consists of a vertical force makes such methods efficient for gravity compensation and a spectrum of action of the robot where process forces act mainly along the direction of gravity.

Category 2: The second category of methods involve the use of a mass suspended to a mechanical lever-arm combined with metrology measurements [34–39]. Compared to the first category of methods, the presence of the lever-arm allows the addition of a torque at the TCP. These passive methods have the advantage of low invasiveness around the robotic system. On the other hand, the applied force at the TCP is still limited to a purely vertical force. Such methods might also require more attention for the management of mechanical interferences in production settings due to the presence of the lever-arm and suspended mass, which might further impose in some cases the removal of production toolings and/or clamping tables to calibrate the robot in its production-relevant work volume.

Category 3: As part of the third family of methods, several works make use of a unidirectional force generator between the robot end-effector and a fixed location in the robot environment, combined with metrology measurements. Most references in this category have adopted a cable connection between the robot and a vertically-guided mass, by means of an pulley mass system or a mass guided in a vertical cage [20,23,40–42]. The authors in [27,43] realize similar load cases with a Loaded Double Ball Bar (LDBB). These methods offer the advantage of achieving non-vertical force vectors. However, for a given robot pose, only one direction of loading is possible, which has the effect of specializing the growth of the robot accuracy for process forces pointing in these directions. In order to overcome this limitation, [42] proposes to manually relocate the pulley system to several locations around the robot, at the expense of a greater invasiveness in production settings and a decrease in the possible degree of automation of the method.

Category 4: Refs. [14,44–46] introduce the use of a docking station to clamp the robot to the environment, offering the advantage of loading the robot, during calibration, with any combined force/torque load case within its actuator torque capability. Another advantage is that the method does not rely on any external measurement, as long as the structure used for docking is sufficiently rigid. On the other hand, for a given location of the docking station, only one robot pose is possible, which has the effect of specializing the growth of the robot accuracy in the volume surrounding the docking station. In order to overcome this limitation, [46] proposes to relocate the docking station using a rigid parallel robot (Stewart platform), at the expense of a greater invasiveness in production settings. Such use of a secondary robot for applying load cases intersects the methods in the fifth category hereafter.

Category 5: This category of methods involve the use of a computer-controlled secondary 6-degree-of-freedom robot to exert multidirectional load cases at the TCP of the robot being calibrated [11,12,46–48]. Such methods allow the generation of elaborated multidirectional load cases over a large workspace through a fully automated sequence. They are therefore ideal candidate platforms for the elastic calibration of robots coming out of the factories of robot manufacturers. On the other hand, due to the presence of a second robot, such methods involve an increased level of invasiveness and deployment complexity for the calibration and recertification of robots in production settings.

In light of the gap highlighted in this review and echoed by Fig. 1, the contributions of this paper with respect to the state-of-the-art involve:

- Introducing a novel in-situ elastic robot calibration (IREC) apparatus and method allowing to conciliate requirements of low invasiveness, for seamless deployment in industrial settings in the presence of all the production hardware, combined with the capability to generate multidirectional calibration load cases over a production-relevant workspace (Section 2).
- Introducing a new technique for the generation of calibration poses that minimizes a metric surface cover index. Compared to best-in-class methods, this pose search heuristics provides faster execution times together with smoother and faster convergences in the context of the IREC protocol (Section 3.1).
- Presenting a novel monitoring tool, called *accuracy competency development charts* (Codecs), which is the graphical output of a repeated cross-validation algorithm. This statistical algorithm allows visualizing how the accuracy of deviation under load prediction grows during the calibration as a function of the number and distribution of calibration poses, and how this growth is influenced by the complexity of the load cases and that of the elastic model (Section 3.2).
- Two case studies are presented in Section 4 to show the generality of the proposed method and algorithms, first the robotized automated fiber placement (AFP) processing of a 3D thermoplastic aerostructure and subsequently the robotized machining of a representative primary aluminium aerospace part. In both cases, the calibrated elastic model has been successfully implemented in a Linux Xenomai real-time target in order to compensate elastic deviations induced by process forces in real-time.

2. Apparatus and methodology for in-situ robot elastic calibration

2.1. Requirements for in-situ elastic calibration

In order to respond to the need for an elastic calibration method that would conciliate requirements of minimal invasiveness and maximal coherence with the spectrum of action of the robot, a key functional requirement that we have established has been the need to be able to calibrate the robot with all its production hardware. This ensured that the elastic calibration process would be capable of capturing all possible physical phenomena contributing to the Cartesian structural behavior of the production platform during production, including the structural behavior of i. the process end-effector, ii. the force sensor (when present to measure process forces), iii. external axi(e)s on which the robot could possibly be mounted as well as iv. the concrete floor supporting the motion platform in the production environment.

Subsequently, a pivotal idea in the formulation of the calibration method has been that production toolings should be leveraged in the robot calibration process. The rationale behind this added functional requirement is that toolings provide physical embodiments of the spectrum of action of the robot in production settings, in terms of geometric location of process trajectories in the robot workspace but also specification of the loci where interaction forces occur between the robot and the part(s) being processed. Furthermore, production toolings are also readily available in the production environment to support a physical interaction with the robot during the calibration. The later are designed to sustain process loads, thus allowing, during the calibration, the development of load cases that can be very coherent with those stemming from the production process. In fine, the use of toolings offers the possibility to obtain a specialization of the robot competency under load where it is needed during manufacturing tasks, ensuring that the robotic equipment is offering maximal value during production.

2.2. Elastic calibration apparatus and method

The federation of the two aforementioned requirements with the requirements of minimal invasiveness and high degree of automation

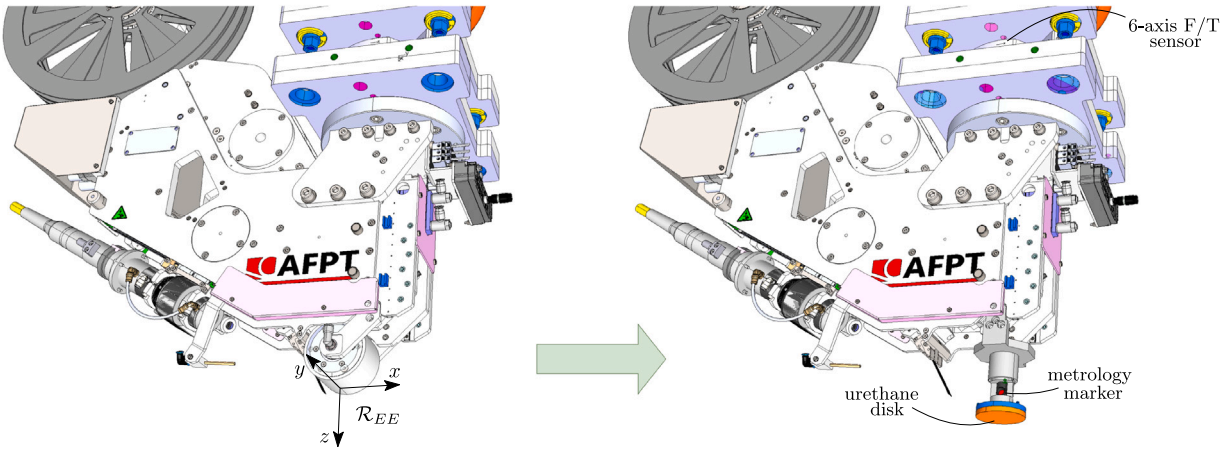

(a) Installation of calibration apparatus in lieu of AFP compaction roller

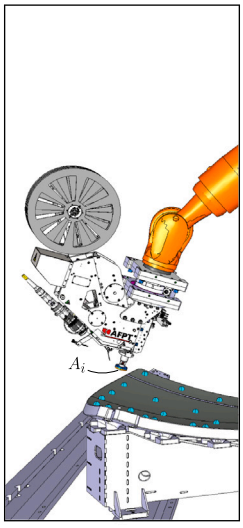

(b) Approach pose A_i, with $i = 1$ to N

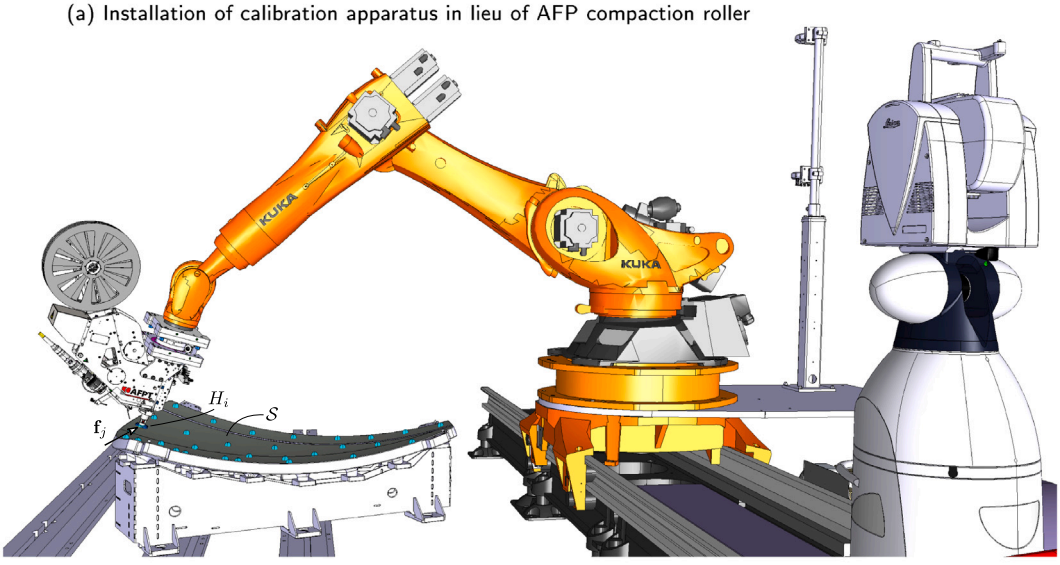

(c) After it moves to just a few millimeters away from pose H_i on surface S, the robot is commanded to achieve a series of controlled load cases $\mathbf{f}_j$, $j = 1$ to M, while remaining into tribological engagement with the surface.

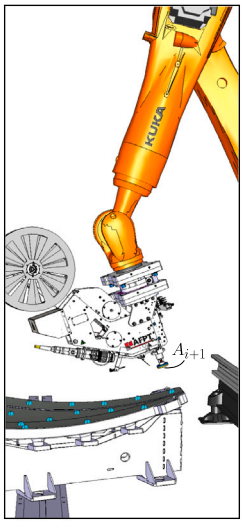

(d) Approach pose A_{i+1}

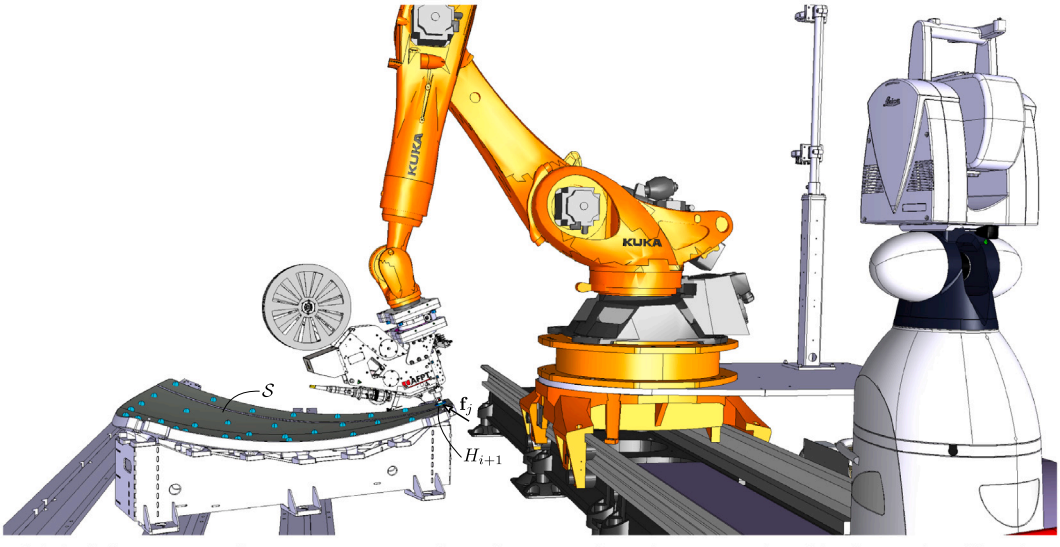

(e) And the corresponding engagement configuration H_{i+1} where the same series of load cases is achieved.

Fig. 2. Illustration of the in-situ robot elastic calibration (IREC) apparatus and method. The cyan spheres represent a set of $N = 31$ engagement poses, generated with the k-vertex Gon COVER heuristics (ref. Section 3.1.2) that are reachable by the robot, allow a clean engagement on the surface S and are exempt from any kinematic singularities, while the robot TCP's z-axis is normal to the surface. The engagement poses shown in subfigures (b,c) and (d,e) thereby illustrate 2 of these 31 poses.

led us to the formulation of the apparatus and method that are illustrated in Fig. 2, where our notations for relevant frames, points, vectors and matrices are introduced, complemented by Procedure 1 providing more details about each step. Fig. 2(a) shows the calibration apparatus mounted in lieu of the compaction roller of a robotized AFP process end-effector. As it can be seen in Fig. 2(b–e), the technique involves soliciting a movement of the robot in force control mode in a direction that is resisted tribologically by the constraint, the production mold used for layup of composite fibers in this case, until a stable load case is achieved, measuring a variation in position of the robot during the resisted movement, and associating the variation in position with a magnitude of the force in the tribologically-resisted direction. The method is repeated for a series of load cases in a multitude of engagement configurations against the constraint (more details about this industrial aerospace case study are provided in Section 4.2). It is noteworthy that the extremity of the calibration apparatus incorporates an aggregated disk made of a more compliant material – urethane has been our material of choice – that promotes the tribological contact while avoiding marking or material transfer with the surface of the constraint.

Procedure 1. In-situ robot elastic calibration (IREC)

Input: Known set of engagement configurations H_i of the robot end with constraint surface S, for $i = 1$ to N.
Known set of load cases $\mathbf{f}_j$, for $j = 1$ to M.
Result: 3-D arrays $\mathbf{P}^c$, $\mathbf{P}^m$ and $\mathbf{F}^m$ with dimensions $(N \times M \times 3)$ and 3-D array $\boldsymbol{\Theta}^m$ with dimensions $(N \times M \times 6)$

Initialize 3-D arrays $\mathbf{P}^c$, $\mathbf{P}^m$, $\mathbf{F}^m$ and $\boldsymbol{\Theta}^c$
$i \leftarrow 1$
while $i \leq N$ **do** /* Sweep of engagement poses */
  Robot in HOME configuration
  Move robot to approach/retract pose A_i
  Move robot in the direction of contact pose H_i
  Stop robot a few millimeters before contact
  Record TCP position $\mathbf{p}^c_{i0}$ provided by controller
  Record marker position $\mathbf{p}^m_{i0}$ measured by metrology
  Set robot in force control mode along X,Y,Z axes
  $j \leftarrow 1$
  while $j \leq M$ **do** /* Sweep of load cases */
    Establish tribologically-resisted load case $\mathbf{f}_j$
    Record load case $\mathbf{f}^m_{ij}$ measured by force sensor
    Record TCP position $\mathbf{p}^c_{ij}$ provided by controller
    Record joint angles $\boldsymbol{\theta}^c_{ij}$ provided by controller
    Record metrology marker position $\mathbf{p}^m_{ij}$
    $\mathbf{P}^c[i,j,:] \leftarrow \mathbf{p}^c_{ij} - \mathbf{p}^c_{i0}$
    $\boldsymbol{\Theta}^c[i,j,:] \leftarrow \boldsymbol{\theta}^c_{ij}$
    $\mathbf{P}^m[i,j,:] \leftarrow \mathbf{p}^m_{ij} - \mathbf{p}^m_{i0}$
    $\mathbf{F}^m[i,j,:] \leftarrow \mathbf{f}^m_{ij}$
    $j \leftarrow j + 1$
  end while
  Set robot controller back in position control mode
  Move robot back to approach/retract pose A_i
  $i \leftarrow i + 1$
end while

Another key component of the elastic calibration apparatus is the integration of a laser tracker metrology marker very close to the engagement area. This has been done with the objective of capturing four different phenomena: 1. the small displacement of the robot from its location a few millimeters before contact until it contacts the constraint, 2. the small deformation of the friction bearing disk induced by each load case, 3. micro-slippage that could occur at the contact interface while load cases are being built and 4. any deformation of the constraint itself. Capturing and subtracting these four displacements from the controller-recorded displacement is instrumental in achieving high fidelity force–displacement relationships with the presented procedure.

In Procedure 1, for any array $\mathbf{A}$, the notation $(:)$ in $\mathbf{A}(i,j,:)$ refers to as the vector whose elements are indexed by subscripts $(i,j,1)$ to (i,j,n), where n is the number of pages in the array [49].

In applications involving the use of a spindle and rotating tool, such as machining, finishing, drilling or friction stir welding, the calibration tool can be designed with the compatible interface (HSK, conical, etc.) to allow a rapid tool change in replacement of the process tool. Our second case study will highlight this embodiment in the case of the elastic calibration of a robotized machining platform in Section 4.3. In this case, the constraint used for the elastic calibration was the parallelepiped-shaped block of rough material before material removal. The block of rough material spans precisely the volume of the robot's workspace where accuracy is needed during machining operations.

The aforementioned apparatus and method for in-situ robot elastic calibration were the subject of patent [50].

2.3. General elastic parameter observation system using a lumped kinetostatic model

Since its introduction by Zhang and Gosselin [51–53] to model the stiffness behavior of parallel robots with passive constraining legs, the *lumped kinetostatic model* has offered an efficient modeling technique to account for the structural behavior of robotic mechanical systems with flexibilities. This kinetostatic modeling technique, also referred to as the *virtual joint method* in the literature, makes use of the introduction of additional virtual revolute joints with torsional flexibilities orthogonal to the actuator's axes of rotation. These flexibilities provide the advantage of increasing the kinetostatic fidelity of the previously commonly used model involving torsional flexibilities about the axes of rotation of actuated joints only. This modeling technique was later employed for the kinetostatic modeling of serial industrial robots in [54], as well as in several other works in subsequent years, with a varying number of virtual revolute joints. A lumped kinetostatic model is used to build our elastic parameter observation system in this paper.

2.3.1. Deformation induced by tribologically-resisted load case

The instantaneous kinematic equations of a serial kinematic chain containing n_a actuated and n_v virtual revolute joints can be written in the general form

$$\mathbf{t} \equiv \begin{bmatrix} \boldsymbol{\omega} \\ \dot{\mathbf{p}} \end{bmatrix} = \mathbf{J}_a \dot{\boldsymbol{\theta}}_a + \mathbf{J}_v \dot{\boldsymbol{\theta}}_v = \begin{bmatrix} \mathbf{J}_a & \mathbf{J}_v \end{bmatrix} \begin{bmatrix} \dot{\boldsymbol{\theta}}_a \\ \dot{\boldsymbol{\theta}}_v \end{bmatrix}, \tag{1}$$

where vectors $\mathbf{t}$, $\boldsymbol{\omega}$ and $\dot{\mathbf{p}}$ represent the twist, angular velocity and translational velocity of the end-effector, respectively. Vectors $\dot{\boldsymbol{\theta}}_a$ and $\dot{\boldsymbol{\theta}}_v$ contains the angular velocities about the axes of the actuated and virtual joints. Jacobian matrices $\mathbf{J}_a$ and $\mathbf{J}_v$ are $(6 \times n_a)$- and $(6 \times n_v)$-dimensional matrices whose ith columns, noted $\mathbf{j}_{i_a}$ and $\mathbf{j}_{i_v}$, take the standard form [55]

$$\mathbf{j}_{i_a} = \begin{bmatrix} \mathbf{e}_{i_a} \\ \mathbf{e}_{i_a} \times \mathbf{r}_{i_a} \end{bmatrix} \quad \text{and} \quad \mathbf{j}_{i_v} = \begin{bmatrix} \mathbf{e}_{i_v} \\ \mathbf{e}_{i_v} \times \mathbf{r}_{i_v} \end{bmatrix}. \tag{2}$$

In Eq. (2), vectors $\mathbf{e}_{i_a}$ and $\mathbf{e}_{i_v}$ are unit vectors in the direction of their associated actuated and virtual joint axes. Vectors $\mathbf{r}_{i_a}$ and $\mathbf{r}_{i_v}$ are defined as the vectors joining the origins of the revolute joint axes (in the Hartenberg–Denavit notation) to the tool-center-point (TCP) of the robot end-effector.

For small deformations induced by an external wrench consisting of a pure tribologically-resisted force $\mathbf{f}_{tres}$ applied on the end-effector, we can rewrite the translational part of instantaneous kinematic Eqs. (1) in the form

$$\delta\mathbf{p} = \begin{bmatrix} \mathbf{J}_{t_a} & \mathbf{J}_{t_v} \end{bmatrix} \begin{bmatrix} \delta\boldsymbol{\theta}_a \\ \delta\boldsymbol{\theta}_v \end{bmatrix}, \tag{3}$$

where $\delta\mathbf{p}$ is the induced small deformation at the TCP and $\delta\boldsymbol{\theta}_a$ and $\delta\boldsymbol{\theta}_v$ are the corresponding small axial torsional deformations. Jacobian matrices $\mathbf{J}_{t_a}$ and $\mathbf{J}_{t_v}$ are $(3\times n_a)$- and $(3\times n_v)$-dimensional matrices whose

ith columns contain respectively the last three elements of $\mathbf{j}_{i_a}$ and the last three elements of $\mathbf{j}_{i_v}$, as defined in Eq. (2).

Let us introduce square compliance matrices $\mathbf{C}_a$ and $\mathbf{C}_v$ whose diagonal elements are respectively the compliances of the n_a actuated and n_v virtual joints. If we define torque vectors $\boldsymbol{\tau}_a$ and $\boldsymbol{\tau}_v$ whose elements are the torques induced by the tribologically-resisted force $\mathbf{f}_{tres}$ about the actuated and virtual joints, we can write

$$\begin{bmatrix}\delta\boldsymbol{\theta}_a\\ \delta\boldsymbol{\theta}_v\end{bmatrix} = \begin{bmatrix}\mathbf{C}_a & \mathbf{0}\\ \mathbf{0} & \mathbf{C}_v\end{bmatrix}\begin{bmatrix}\boldsymbol{\tau}_a\\ \boldsymbol{\tau}_v\end{bmatrix}. \tag{4}$$

It is noteworthy that we have purposefully not included the gravitational effects in Eq. (4). The reason is that during the calibration process we are solely observing the deformation induced by the tribologically-resisted force $\mathbf{f}_{tres}$. At each engagement pose, the robot is already pre-deformed by the gravitational effects before the calibration procedure starts and no additional deformation is stemming from gravitational effects during each series of controlled load cases. Accordingly, we have defined vectors $\delta\mathbf{p}$, $\delta\boldsymbol{\theta}_a$ and $\delta\boldsymbol{\theta}_v$ to be solely associated with deformations induced by the tribologically-resisted load cases. Now substituting the vector of small articular torsional deformations in Eq. (3) using Eq. (4), we obtain

$$\delta\mathbf{p} = \left[\mathbf{J}_{t_a}\mathbf{C}_a \;\middle|\; \mathbf{J}_{t_v}\mathbf{C}_v\right]\begin{bmatrix}\boldsymbol{\tau}_a\\ \boldsymbol{\tau}_v\end{bmatrix}. \tag{5}$$

By virtue of the principle of virtual work, one can write

$$\mathbf{f}_{tres}^{\mathrm{T}}\delta\mathbf{p} = \boldsymbol{\tau}_a^{\mathrm{T}}\delta\boldsymbol{\theta}_a + \boldsymbol{\tau}_v^{\mathrm{T}}\delta\boldsymbol{\theta}_v = \begin{bmatrix}\boldsymbol{\tau}_a^{\mathrm{T}} & \boldsymbol{\tau}_v^{\mathrm{T}}\end{bmatrix}\begin{bmatrix}\delta\boldsymbol{\theta}_a\\ \delta\boldsymbol{\theta}_v\end{bmatrix}. \tag{6}$$

Substituting the vector of small axial torsional deformations using kinematic relation Eq. (3), we can write

$$\mathbf{f}_{tres}^{\mathrm{T}}\delta\mathbf{p} = \begin{bmatrix}\boldsymbol{\tau}_a^{\mathrm{T}} & \boldsymbol{\tau}_v^{\mathrm{T}}\end{bmatrix}\begin{bmatrix}\mathbf{J}_{t_a} & \mathbf{J}_{t_v}\end{bmatrix}^{-1}\delta\mathbf{p}. \tag{7}$$

Since Eq. (7) is valid for any value of $\delta\mathbf{p}$, we obtain

$$\mathbf{f}_{tres}^{\mathrm{T}} = \begin{bmatrix}\boldsymbol{\tau}_a^{\mathrm{T}} & \boldsymbol{\tau}_v^{\mathrm{T}}\end{bmatrix}\begin{bmatrix}\mathbf{J}_{t_a} & \mathbf{J}_{t_v}\end{bmatrix}^{-1}, \tag{8}$$

an expression that, once transposed, yields to the relation

$$\begin{bmatrix}\boldsymbol{\tau}_a\\ \boldsymbol{\tau}_v\end{bmatrix} = \begin{bmatrix}\mathbf{J}_{t_a} & \mathbf{J}_{t_v}\end{bmatrix}^{\mathrm{T}}\mathbf{f}_{tres}. \tag{9}$$

Substituting the vector of joint torques in Eq. (5) using Eq. (9), we obtain the sought general kinetostatic relation expressing the small deformation $\delta\mathbf{p}$ at the TCP induced by the tribologically-resisted force $\mathbf{f}_{tres}$

$$\delta\mathbf{p} = \left[\mathbf{J}_{t_a}\mathbf{C}_a \;\middle|\; \mathbf{J}_{t_v}\mathbf{C}_v\right]\begin{bmatrix}\mathbf{J}_{t_a} & \mathbf{J}_{t_v}\end{bmatrix}^{\mathrm{T}}\mathbf{f}_{tres}. \tag{10}$$

Relation (10) is valid for any arrangement and number of actuated and passive joints in the serial kinematic chain.

2.3.2. Observation system using data arrays recorded during the elastic calibration

In order to derive a matrix relation allowing us to observe all the compliances of the serial kinematic chain, we define n_a-dimensional vector $\mathbf{c}_a$ and n_v-dimensional vector $\mathbf{c}_v$ as the vectors whose elements are respectively the compliances of the n_a actuated and n_v virtual joints, we can rearrange Eq. (10) in the more convenient form

$$\delta\mathbf{p} = \left[\mathbf{J}_{t_a}\mathbf{diag}\left(\mathbf{J}_{t_a}^{\mathrm{T}}\mathbf{f}_{tres}\right) \;\middle|\; \mathbf{J}_{t_v}\mathbf{diag}\left(\mathbf{J}_{t_v}^{\mathrm{T}}\mathbf{f}_{tres}\right)\right]\begin{bmatrix}\mathbf{c}_a\\ \mathbf{c}_v\end{bmatrix}, \tag{11}$$

where, for any n-dimensional vector $\mathbf{v}$, matrix $\mathbf{diag}(\mathbf{v})$ is defined as the $(n\times n)$ square matrix whose diagonal elements are the elements of $\mathbf{v}$.

Now correlating the small deformation $\delta\mathbf{p}$ at the TCP with vector quantities that are either recorded or measured during the IREC procedure after establishment of the tribologically-resisted load case $\mathbf{f}_{ij}$, we can write

$$\underbrace{\mathbf{p}_{ij}^{c} - \mathbf{p}_{i0}^{c}}_{a} = \delta\mathbf{p}_{ij} + \underbrace{\mathbf{p}_{ij}^{m} - \mathbf{p}_{i0}^{m}}_{b}, \tag{12}$$

which expresses the fact that the controller commanded displacement (quantity a) transfers in part into the small deformation $\delta\mathbf{p}_{ij}$ as well as into a physical displacement (quantity b) that is captured using the external metrology equipment. In order to integrate data arrays recorded during the calibration, Eq. (12) is rewritten as

$$\delta\mathbf{p}_{ij} = \mathbf{P}^{c}[i,j,:] - \mathbf{P}^{m}[i,j,:]. \tag{13}$$

Now substituting the small TCP deformation of Eq. (13) into Eq. (11), and integrating the load case recorded during the IREC procedure in the resulting expression, we obtain

$$\begin{aligned}&\mathbf{P}^{c}[i,j,:] - \mathbf{P}^{m}[i,j,:] =\\ &\left[\mathbf{J}_{t_a}^{ij}\mathbf{diag}\left([\mathbf{J}_{t_a}^{ij}]^{\mathrm{T}}\mathbf{F}^{m}[i,j,:]\right) \;\middle|\; \mathbf{J}_{t_v}^{ij}\mathbf{diag}\left([\mathbf{J}_{t_v}^{ij}]^{\mathrm{T}}\mathbf{F}^{m}[i,j,:]\right)\right]\begin{bmatrix}\mathbf{c}_a\\ \mathbf{c}_v\end{bmatrix}\end{aligned} \tag{14}$$

where Jacobian matrices $\mathbf{J}_{t_a}$ and $\mathbf{J}_{t_v}$ are evaluated for the actuated joint configuration $\boldsymbol{\Theta}^{c}[i,j,:]$ recorded after stabilization of tribologically-resisted load case $\mathbf{f}_{ij}$. Considering that the IREC procedure involves N engagement poses with M load cases at each pose, we obtain the observation system

$$\mathbf{d} = \begin{bmatrix}\mathbf{O}_a & \mathbf{O}_v\end{bmatrix}\begin{bmatrix}\mathbf{c}_a\\ \mathbf{c}_v\end{bmatrix}, \tag{15}$$

in which the deformation vector $\mathbf{d}$ and observation matrices $\mathbf{O}_a$ and $\mathbf{O}_v$ are given by

$$\mathbf{d} \equiv \begin{bmatrix}\mathbf{P}^{c}[1,1,:] - \mathbf{P}^{m}[1,1,:]\\ \vdots\\ \mathbf{P}^{c}[N,M,:] - \mathbf{P}^{m}[N,M,:]\end{bmatrix}, \tag{16}$$

$$\mathbf{O}_a \equiv \begin{bmatrix}\mathbf{J}_{t_a}^{11}\mathbf{diag}\left([\mathbf{J}_{t_a}^{11}]^{\mathrm{T}}\mathbf{F}^{m}[1,1,:]\right)\\ \vdots\\ \mathbf{J}_{t_a}^{NM}\mathbf{diag}\left([\mathbf{J}_{t_a}^{NM}]^{\mathrm{T}}\mathbf{F}^{m}[N,M,:]\right)\end{bmatrix}, \tag{17}$$

$$\mathbf{O}_v \equiv \begin{bmatrix}\mathbf{J}_{t_v}^{11}\mathbf{diag}\left([\mathbf{J}_{t_v}^{11}]^{\mathrm{T}}\mathbf{F}^{m}[1,1,:]\right)\\ \vdots\\ \mathbf{J}_{t_v}^{NM}\mathbf{diag}\left([\mathbf{J}_{t_v}^{NM}]^{\mathrm{T}}\mathbf{F}^{m}[N,M,:]\right)\end{bmatrix}. \tag{18}$$

The observation system in Eq. (15) is an overdetermined linear system of $N\times M\times 3$ equations with $n_a + n_v$ unknowns. Solving this system for compliance vectors $\mathbf{c}_a$ and $\mathbf{c}_v$ is equivalent to solving a standard least-squares curve fitting problem of the form

$$\min_{\mathbf{c}_a,\mathbf{c}_v}\left\langle\frac{1}{2}\left\|\begin{bmatrix}\mathbf{O}_a & \mathbf{O}_v\end{bmatrix}\begin{bmatrix}\mathbf{c}_a\\ \mathbf{c}_v\end{bmatrix} - \mathbf{d}\right\|_2^2\right\rangle. \tag{19}$$

The specific arrangement of actuated and virtual joints that we have selected in our lumped kinetostatic model will be presented in Section 4 in which we present aerospace case studies. The mathematical solver implemented for solving Eq. (19) will be discussed in that same section.

3. Enabling software technologies for the IREC procedure

The IREC procedure needs to anchor on a set of calibration poses that can efficiently support a growth of the accuracy of the robot under load throughout its spectrum of action in production. While a set of poses including a large population of randomly-distributed poses throughout the surface of the constraint might appear to be a candidate approach, the set of poses should actually be reduced as much as possible in order for the calibration process to exhibit a minimized cycle-time and our proposed statistical cross-validation technique to be computationally efficient and of practical use.

3.1. Automated generation of calibration poses

A review of the pose search techniques proposed in the art for robot calibration, that we conducted at the beginning of this research, highlighted the fact that a relative consensus had emerged concerning the fact that the use of observability index O_1, as defined in [56], in

combination with the DETMAX exchange algorithm [57] was shown to yield the best results in a range of calibration applications ranging from the geometric calibration of parallel robots [58] to the geometric [59] and elastic [47] calibration of serial industrial robots.

3.1.1. Investigation of O_1 DETMAX algorithm

Based on these findings in the art, we made the choice to first explore the O_1 DETMAX algorithm in the context of the IREC calibration procedure. Let $Y^N \equiv \{\xi^1, \xi^2, \ldots, \xi^N\}$ denote the set of N engagement configurations ξ^i against the surface S during the calibration. We can therefore define observability index O_1 for a given set of poses Y^N as

$$O_1(Y^N) = \frac{\sqrt[n_a+n_v]{\sigma_{n_a+n_v} \cdots \sigma_2 \sigma_1}}{\sqrt{3NM}}, \tag{20}$$

where σ_i is the ith singular value obtained from the singular-value-decomposition of observation matrix $\begin{bmatrix}\mathbf{O}_a & \mathbf{O}_v\end{bmatrix}$ given by Eqs. (15), (17), (18).

Now considering that a large pool of calibration poses has been generated on the surface of the constraint S, we define Ω as the subset of this pool of configurations that are reachable by the robot when its TCP z-axis is normal to S. Using these notations, we implemented the Iterative One-by-one Pose Search (IOOPS) algorithm proposed by Daney at al. [58] in the context of the IREC calibration. Pseudocode 1 describes our implementation of this algorithm.

Pseudocode 1. O_1 DETMAX (IOOPS) for IREC method

Input: Pool of calibration poses Ω randomly distributed throughout surface of constraint S that are reachable by the robot, allow a clean engagement on the surface and are exempt from any kinematic singularities, while the robot TCP's z-axis is normal to S for all the poses.
Specified number N of calibration poses.
Result: Set of N optimized parameter configurations Y^N.

```
Randomly select an initial set of poses Y^N in Ω
repeat
    Find ξ+ in (Ω \ Y^N) that maximizes O1(Y^N ∪ ξ+)
    Y^{N+1} ← Y^N ∪ ξ+
    Find ξ− in (Y^{N+1}) that maximizes O1(Y^{N+1} \ ξ−)
    Y^N ← Y^{N+1} \ ξ−
until (ξ+ = ξ−)
```

In order to illustrate a practical implementation of this pseudocode, we considered the case of the robotic AFP test-bed and double-curvature tooling that we have used to illustrate the IREC procedure in Fig. 2. A pool of 3000 poses were randomly generated on the surface of the tooling for which reachability of the robot TCP and absence of kinematic singularities could be confirmed for the entire population. The pool of 3000 poses as well as the IOOPS-computed reduced set of calibration poses appear respectively as small black circles and red squares in Fig. 3 (the choice for $N = 31$ calibration poses was made to compare the IOOPS results with those obtained with the proposed metric k-vertex cover pose search heuristics, as we explain later in Section 3.1.2).

While using index O_1 in conjunction with the IOOPS algorithm is a well-documented solution to ensure the numerical conditioning of the observation matrix and the achievement of important precision improvements in robot calibration applications over relatively large workspaces, Fig. 3 shows, in the context of the IREC method, a clustering of the poses in the vicinity of the vertices of the tooling's surface, as well as a peripheralization of the poses towards the edges of the surface, behaviors that were already observed and discussed by the authors in [58]. Moreover, the IOOPS algorithm involves calculating the eigenvalues of the observability matrix at each iteration until the algorithm converges, which is highly computationally-intensive.

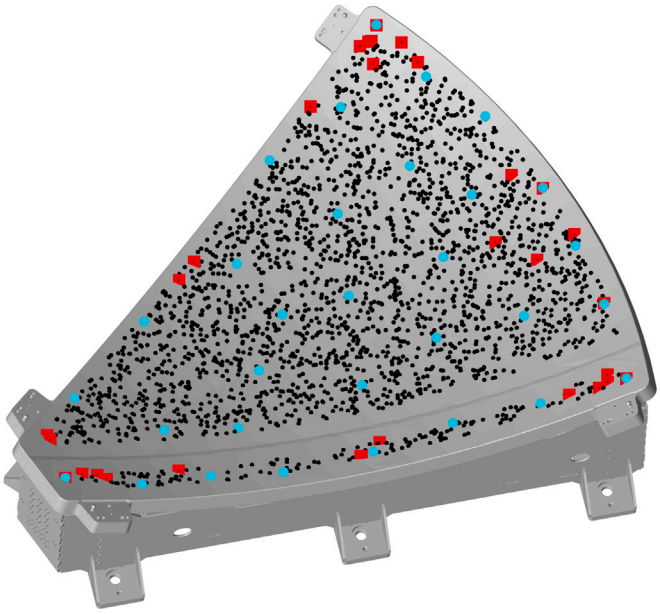

Fig. 3. Illustration of the deployment of the IOOPS and COVER pose search techniques in the case of the robotic AFP test-bed and double-curvature tooling surface used to illustrate the IREC procedure in Fig. 2. The pool of 3000 candidate poses, as well as IOOPS- and COVER-computed sets of 31 calibration poses appear as small black circles, red squares and cyan circles, respectively. The robot and process end-effector with calibration apparatus are set-up as shown in Fig. 2. They are not shown to maximize the readability of the figure.

Considering that our main objectives was to exploit a pose search technique that would involve a reduced set of poses for integration in a statistical cross-validation scheme, would be computationally light, while providing a very good representation of the spectrum of action of the robot in production, we thought that is would be worthwhile investigating the potential of purely geometric approaches. This rationale is reinforced by the fact that the IREC method exploits poses on localized surfaces in the robot's workspace.

It is noteworthy that a more recent research showed that elastic calibration results could be further improved by using a D-optimal design of experiment instead of the O_1 observability index in conjunction with the DETMAX algorithm [48]. The research works pertaining to calibration pose search techniques presented in our paper were conducted for the most part prior to that publication and we have not explored the potential of the use of D-optimality in the context of the IREC calibration procedure.

3.1.2. Cover-based pose search heuristics

The first metric surface cover technique that we investigated was the projection of a regular planar surface mesh along a given direction to generate a landmark on the double-curvature surface of the constraint S. While relatively computationally light, the method had the disadvantage of generating distorted landmarks on the surface of the constraint which lowered its effectiveness to effectively represent the spectrum of action of the robot in production. This phenomenon was aggravated in the case of convex or concave surfaces with important curvatures. In such cases, shadow effects had to be considered and required the projection of meshes along several directions to cover the entire surface S, which also complexed the method significantly.

In order to make sure the method would be automatable and generalizable to surfaces with important curvatures while still remaining computationally light, we then investigated heuristics proposed in the literature for solving the classical vertex k-center problem. This problem, as illustrated in Fig. 4, consists in finding a subset $Y^k \subseteq \Omega$ of k

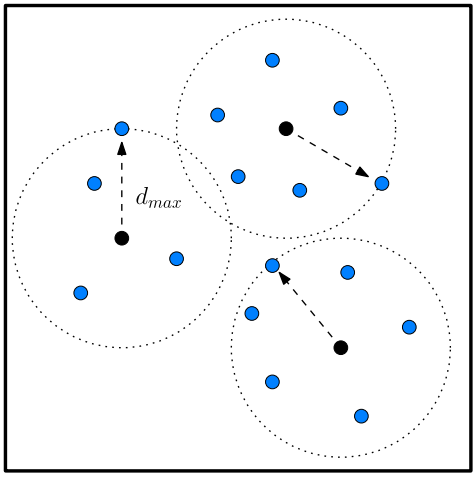

Fig. 4. Schematic illustration of the vertex k-center problem. This problem consists in finding a subset $Y^k \subseteq \Omega$ of k vertices (here the $k = 3$ vertices are represented by black circles) in a metric space such that the distance d_{max} from the farthest vertex in Ω (the pool of vertices in Ω is represented by blue circles) to its nearest center in Y^k is minimized.

vertices in a metric space such that the distance d_{max} from the farthest vertex in Ω to its nearest center in Y^k is minimized. This problem has typical applications in facility location and clustering. The reader is referred to the Ref. [60] for a thorough survey and experimental comparison of the most important heuristics, metaheuristics, approximation algorithms, and exact algorithms that have been proposed in the literature to solve this problem.

In the specific context of the IREC method, a solution to the vertex k-center problem would have the advantage of providing an optimal cover of the robot's spectrum of action in production with a minimal set of poses. Instead of a priori arbitrarily defining a number of poses N, that may or may not be a sufficient quantity of calibration poses to maximize the accuracy of the robot in its production tasks, we can define a cover distance d_{max} that will stop the algorithm at a calculated number of poses that will guarantee a certain quality of cover of the constraint's surface S.

In this perspective, taking into account the experimental comparisons performed in [60], we selected the approximate solution to the vertex k-center problem proposed by Gonzalez [61] due to the fact that it exhibits very acceptable performance while having the lowest complexity, at $O(kn)$, and significantly shorter computational times compared to all the other evaluated algorithms. Our adaptation of the Gon algorithm in the context of the IREC method, that we will refer to as the COVER heuristics in the rest of this paper, is described by Pseudocode 2.

In order to illustrate a practical implementation of this pseudocode and compare it with the IOOPS algorithm, we applied it to the same pool of 3000 poses that we considered in Fig. 3. Through empirical investigation (more details about this analysis are presented in Section 4.2.3), we have found that a practical cover distance for this case study is $d_{max} = 175$ mm. In this case, the COVER heuristics stops at $N = 31$ poses, which explains why we have used this number for the IOOPS algorithm as well. Correspondingly, the COVER-computed reduced set of 31 calibration poses appear as cyan circles in Fig. 3.

Thanks to its ability to efficiently describe the spectrum of action of the robot in production with a reduced set of calibration poses, coupled with its computational efficiency, the COVER pose search heuristics has become our method of choice for all industrial embodiments of the IREC method. Its implementation in our proposed statistical cross-validation method is presented in the following subsection.

Pseudocode 2. Gon heuristics (COVER) for IREC method

Input: Pool of calibration poses Ω randomly distributed throughout surface of constraint S that are reachable by the robot, allow a clean engagement on the surface and are exempt from any kinematic singularities, while the robot TCP's z-axis is normal to S for all the poses.
Specified number N of calibration poses and maximal covering distance threshold d_{max}.
Result: Set of N optimized parameter configurations Y^N or less (in case the threshold d_{max} is reached first).

1: Select first pose ξ_1 that is the closest to the geometric centroid of all the poses in pool Ω
2: $Y^1 \leftarrow \xi_1$
3: $i \leftarrow 1$
4: $k \leftarrow N$
5: **repeat**
6: Find ξ^+ in $(\Omega \setminus Y^i)$ associated with position on S that is the farthest away (at distance d^+) from all points mapped by partial solution set Y^i
$Y^{i+1} \leftarrow Y^i \cup \xi^+$
7: $i \leftarrow i + 1$
8: **until** $(i = k - 1)$ **or** $(d^+ \leq d_{max})$

3.2. Software tool to monitor the growth of accuracy during the calibration

3.2.1. Rationale

The in-situ deployment and automation of calibration technologies, such as the IREC apparatus and method, in industrial environments impose contradictory requirements. On one hand the number of calibration poses has to be minimized to reduce the calibration/recertification cycle-times as much as possible, on the other hand a greater number of poses might further improve the accuracy of the robot, which is of significant value for its production activities.

Furthermore, the way the accuracy competency under load of the robot can develop relies heavily on several key technological pillars. These pillars include, in the specific case of elastic calibration methods, i. the number of calibration poses and their distribution (which is heavily dependent on the pose search technique used), ii. the nature of the load cases used to solicit the robot, as well as iii. the fidelity of the elastic model. Maximal accuracy under load is therefore achievable when these three technological pillars provide a maximal coherence with the deformation physics of the robot and its spectrum of action in production.

In order to answer these requirements, the proposed repeated cross-validation method provides a diagnostics tool that allows meeting the combined objectives of better assessing that degree of coherence while also allowing an informed deliberation concerning the number of calibration poses to use in production settings.

3.2.2. CODEC algorithm

The detailed repeated cross-validation method is presented in Algorithm 1. It exploits the data recorded during execution of the IREC procedure using a set Y^N of N engagement poses against the surface S, previously selected using the COVER heuristics. The choice of the COVER heuristics was made due all the advantages that we have highlighted in Section 3.1, especially its ability to efficiently span the spectrum of action of the robot with a minimal set of poses. Elastic calibration data recorded in COVER-generated poses are therefore very good candidates to generate verification sets in a cross-validation algorithm.

In addition to directly highlighting the influence of the number of calibration poses (size of train set) in Codecs, it is noteworthy that the CODEC algorithm also allows the exploration of the influence of each of the three aforementioned technological pillars through the testing of

– different pose search techniques (at line 10),
– different load case architectures (at line 11, via the entries of array $\mathbf{F}^m$), and
– different deformation physics (at line 11, by changing the model used in Eq. (19)).

Algorithm 1. Accuracy competency development chart (CODEC) using repeated cross-validation

Input: Set $\mathcal{Y}^N$ of N engagement poses against the surface $\mathcal{S}$ selected in pool Ω using the COVER heuristics.
Populated 3-D arrays $\mathbf{P}^c$, $\mathbf{P}^m$, $\mathbf{F}^m$ and $\boldsymbol{\Theta}^m$ following execution of the IREC procedure using set of poses $\mathcal{Y}^N$.
Train/test ratio r defining the chosen ratio, for the cross-validation, between the maximum number of training poses N_c and the number of verification poses N_v.
Maximum number of combinations N_{cv} in training sets.
Result: 3-D compliance arrays $\mathbf{C}_a$, $\mathbf{C}_v$ with respective dimensions $(N_{cv} \times N_c \times n_a)$ and $(N_{cv} \times N_c \times n_v)$.
3-D mean and maximum residual error arrays $\mathbf{E}_\mu$ and $\mathbf{E}_m$ with dimensions $(N_{cv} \times N_c \times 3)$.
Accuracy competency development charts (Codecs).

1: Initialize 3-D arrays $\mathbf{C}_a$, $\mathbf{C}_v$, $\mathbf{E}_\mu$ and $\mathbf{E}_m$
2: $N_c \leftarrow Nr/(r+1)$
3: $N_v \leftarrow N/(r+1)$
4: Determine set $\Omega_{cv}^N \equiv \{\mathcal{Y}_{cv}^1, \ldots, \mathcal{Y}_{cv}^{N_{cv}}\}$ containing N_{cv} combinations of N_v verification poses from $\mathcal{Y}^N$
5: $i \leftarrow 1$
6: **while** $i \leq N_{cv}$ **do** /* Repeated cross-validation */
7: Determine training subset $\mathcal{Y}_{tr}^i \leftarrow \mathcal{Y}^N \setminus \mathcal{Y}_{cv}^i$
8: $j \leftarrow 1$
9: **while** $j \leq N_c$ **do** /* Growing size of train set */
10: Use pose search technique to select subset of j poses $\mathcal{Y}_i^j \equiv \{\boldsymbol{\xi}_i^1, \ldots, \boldsymbol{\xi}_i^j\}$ in subset $\mathcal{Y}_{tr}^i$
11: Determine compliance vectors $\mathbf{c}_a^{ij}$ and $\mathbf{c}_v^{ij}$ by solving Eq. (19) for training subset $\mathcal{Y}_i^j$ using the corresponding entries in 3-D arrays $\mathbf{P}^c$, $\mathbf{P}^m$, $\mathbf{F}^m$ and $\boldsymbol{\Theta}^m$ defined in Procedure 1
12: Validate calibrated model trained with subset $\mathcal{Y}_i^j$ against the data recorded for the current COVER-generated verification set $\mathcal{Y}_{cv}^i$ and store the components of the mean and maximum residual errors in vectors $\boldsymbol{\epsilon}_\mu^{ij}$ and $\boldsymbol{\epsilon}_m^{ij}$
13: $\mathbf{C}_a[i,j,:] \leftarrow \mathbf{c}_a^{ij}$
14: $\mathbf{C}_v[i,j,:] \leftarrow \mathbf{c}_v^{ij}$
15: $\mathbf{E}_\mu[i,j,:] \leftarrow \boldsymbol{\epsilon}_\mu^{ij}$
16: $\mathbf{E}_m[i,j,:] \leftarrow \boldsymbol{\epsilon}_m^{ij}$
17: $j \leftarrow j+1$
18: **end while**
19: $i \leftarrow i+1$
20: **end while**
21: Create Box plots to display the evolutions of the statistical distributions of mean and maximum residual errors (or alternatively those of the identified compliances) as a function of the growing size of the train set, referred to as accuracy competency development charts (Codecs)

Our first case study presented in Section 4.2 will highlight the implementation and benefits of the CODEC algorithm in assessing the influence of these three pillars in the context of the robotized AFP of a 3D aerostructure.

4. Aerospace manufacturing case studies

In this section, we present two case studies that illustrates embodiments of the IREC procedure for deployment in industry, first in the case of the robotized AFP processing of a 3D thermoplastic aerostructure and subsequently in the case of the robotized machining of a representative primary aluminium aerospace part.

4.1. Kinetostatic model, load cases and real-time path correction scheme

The chosen lumped kinetostatic model, as well as the selected solver for the overdetermined observation system, the architecture of the load cases and the real-time path correction scheme are identical for the two case studies.

After comparing several models with different degrees of freedom, we selected an 18 degree of freedom (DOF) lumped kinetostatic model combining $n_a = 6$ torsional elasticities about the axes of the actuated joints with $n_v = 12$ virtual revolute joints in the form of two torsional flexibilities orthogonal to each actuator's axis of rotation. Following an IREC procedure, the 18 compliances are determined in both cases by solving Eq. (19) using the `lsqlin` solver in MATLAB [62]. This 18-DOF kinetostatic model, in which the structural physics of the static balancing mechanism is therefore lumped in the elasticity about the axis of actuator #2, has provided an excellent accuracy performance in our case studies, as it is shown in Sections 4.2 and 4.3.

To complement the kinetostatic model, another key aspect of the IREC procedure pertains to the load cases $\mathbf{f}_j$, $j = 1$ to M, used to solicit the robot at each engagement configuration. Through experimental validation and exploitation of the CODEC algorithm, we found that a very effective way of soliciting the robot was through the achievement of the following set of five (5) tribologically-resisted load cases (expressed locally in the robot TCP frame $\mathcal{R}_{EE}$), i.e.,

1. a load case ${}^1\mathbf{f}_j = [0, 0, f_z]^\mathrm{T}$ normal to surface $\mathcal{S}$,
2. a combined load case ${}^2\mathbf{f}_j = [f_x, 0, f_z]^\mathrm{T}$ (N: North),
3. a combined load case ${}^3\mathbf{f}_j = [-f_x, 0, f_z]^\mathrm{T}$ (S: South),
4. a combined load case ${}^4\mathbf{f}_j = [0, -f_y, f_z]^\mathrm{T}$ (E: East),
5. a combined load case ${}^5\mathbf{f}_j = [0, f_y, f_z]^\mathrm{T}$ (W: West),

in which a positive value of f_z represents a solicitation force normal to the surface pointing in the direction of the robot. The amplitude of the lateral forces are chosen as a function of f_z in load cases NSEW in such a way that the tribological contact between the robot and the constraint remains within the stable Coulomb friction domain. They should also cover the maximal amplitudes of the process forces expected during production while remaining within the allowable maximum continuous torques of all the robot's actuators.

For the two case studies, the robot has been first calibrated using the calibration module of the commercially-available software RoboDK [63]. This calibration includes an identification of the geometric parameters of the robot as well as a kinetostatic model to compensate for gravitational effects. Following calibration, the part programs are corrected in RoboDK using a fake-target method.

The 18-DOF kinetostatic model, once calibrated using the IREC procedure, has been implemented in a real-time path correction control architecture as described in Fig. 5. It is noteworthy that the Force/Torque readings provided in real-time by the ATI Omega 6-axis F/T sensor are processed through a series of filters that not only have the effect of smoothing the signals but also the effect of removing the contributions of the combined weights of the process end-effector and cables. This ensures that the signals sent to the Linux Xenomai RTNet interface correspond to pure 3-dimensional process forces at the robot TCP, thus allowing the 18-DOF kinematic model to compensate solely the deviations that are induced by the manufacturing process (see Fig. 6).

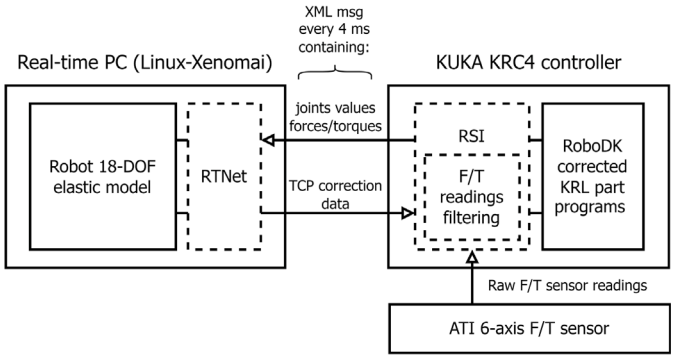

Fig. 5. Architecture for real-time path correction using a 18-DOF kinetostatic model exploiting measured process forces in a Linux Xenomai real-time target.

4.2. Case study #1: Robotized AFP processing of a 3D thermoplastic aerostructure

4.2.1. Robotized T-AFP testbed

The tape laying machine consists of a KUKA KR 120 HA polyarticulated robot, mounted on a rail system and an AFPT MTLH tape laying machine. Each track of 3 × 1/2-inch thermoplastic prepreg tape is deposited by the machine, using a 6 kW laser supplied by Laserline. Its optics shape the beam to a rectangular irradiance profile (see Fig. 6).

The material is fed from spools into the machine's heating zone, where the incoming tape and substrate are melted in front of the nip point of the consolidation roller. A pressure of 6 bar is applied by the conformable, water-cooled compaction roller to ensure intimate contact between the bonding partners. During the melt polymer chains diffuse in the interface of the laminate and tape, thus forming a single unit. Afterwards the cooled roller ensures solidification, before the material cools down to ambient temperature behind the layup machine.

The Thermoplastic Automated Fiber Placement (T-AFP) process with direct consolidation builds a laminate by additively depositing successive tracks and layers [64]. Due to its one-step approach, gaps or overlaps in the laminate cannot be cured by subsequent oven or autoclave post-processes. However, both defects weaken the mechanical performance of a part due to the fiber waviness that occurs when a tape is either placed on top of a previous one or on into a gap. This leads to the requirement to place each track on its predefined position, even for complex parts, and to the need for highly accurate motion kinematics.

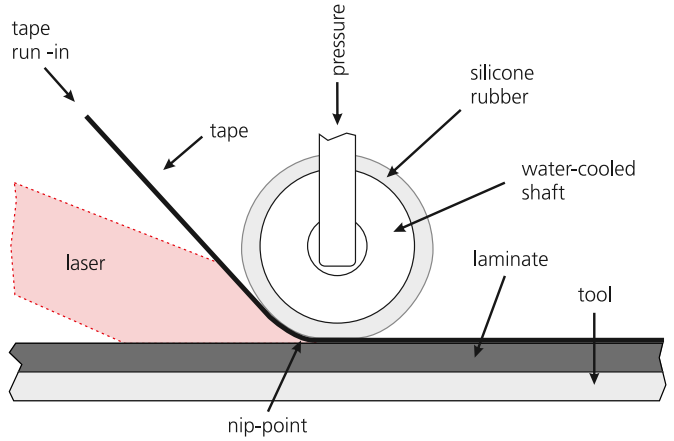

Fig. 6. Schematic description of the T-AFP process.

4.2.2. IREC calibration of T-AFP robotic testbed

An in-situ elastic calibration of the T-AFP robotic test-bed was performed through application of the IREC apparatus and method as described in Section 2.2. Fig. 8(a–f) illustrate the calibration setup as well the first four (4) engagement poses against the T-AFP production mold. Bottom Fig. 8(g) illustrates the calibration output after solving the kinetostatic observation system using Eq. (19) with the 18-DOF kinetostatic model.

It is noteworthy that it would have been possible to further improve the deformation physics in this particular case by modeling the internal deformation of the T-AFP end-effector. However, the accuracy performance that has been obtained during actual deposition of laminates (ref. Fig. 11) was already meeting our $\pm 0,3$ mm tolerance for the maximum elastic side deviation of the robot TCP during rolling motion. This eliminated the justification to further improve the kinetostatic model.

4.2.3. Effect of number and distribution of poses on the growth of accuracy

Having gathered the calibration data during the IREC calibration of the T-AFP robotic workcell described in Fig. 8, we could exploit the CODEC repeated cross-validation algorithm presented in subsection Section 3.2 in order to investigate the influence of the number of calibration poses and their distribution. In this perspective, we chose to compare Codecs obtained by generating train sets using either the IOOPS or the COVER pose search algorithms (by specifying the selected pose-search technique at line 10 of the CODEC algorithm). The resulting Codecs, in which we have used a train/test ratio $r = 70/30$ and maximum number of cross-validations $N_{cv} = N = 31$, are displayed in Fig. 7. They highlight, in the particular case of the IREC method, a smoother and slightly faster stabilization and saturation of the mean and maximum residual errors with the COVER heuristics. Considering how computationally-efficient the COVER heuristics is at $O(kN)$, this

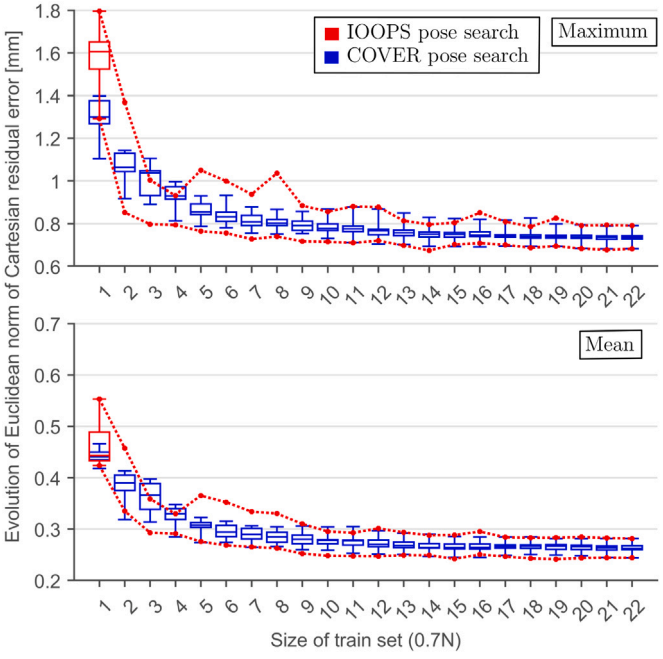

Fig. 7. Accuracy competency development charts constructed using the CODEC algorithm with the dataset obtained during IREC calibration of the T-AFP robotic test-bed with $N = 31$ poses. The two charts illustrate the growth of the mean and maximum robot accuracy as a function of the number of poses in the case of the construction of the train sets using the IOOPS (red) and COVER (blue) pose search algorithms. In both cases, the same combinations of COVER-generated validation sets of $0.3N$ poses, exploiting the five multidirectional load cases ${}^{\ell}\mathbf{f}_j$, $\ell = 1$ to 5, are used to represent the targeted spectrum of action of the robot in production.

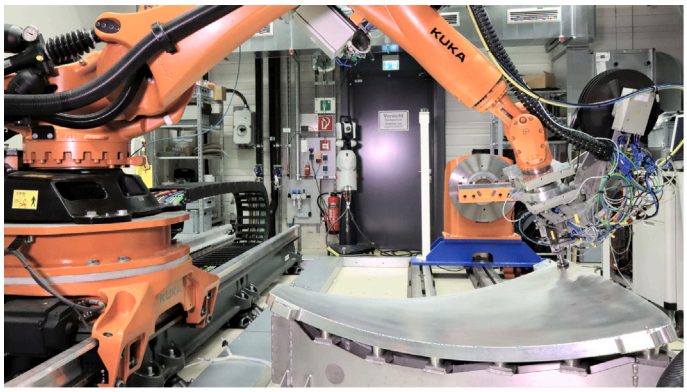

(a) IREC calibration set-up with Leica AT901 Laser Tracker

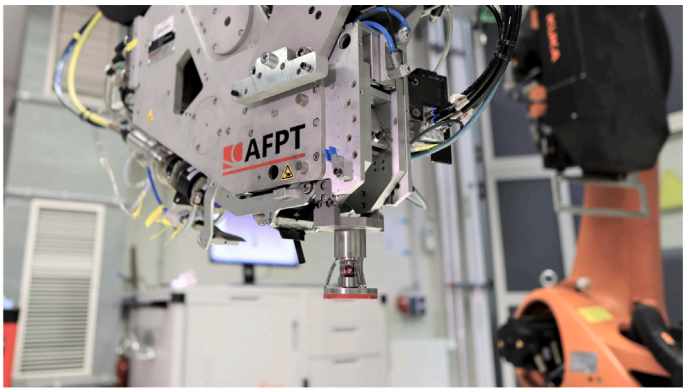

(b) Calibration tool with metrology target and urethane disk (red)

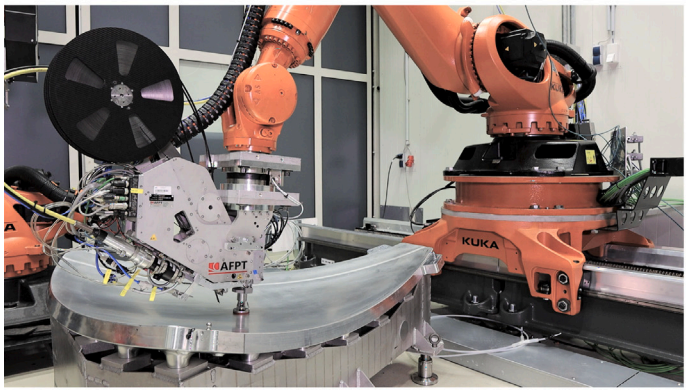

(c) 1st COVER-generated engagement pose

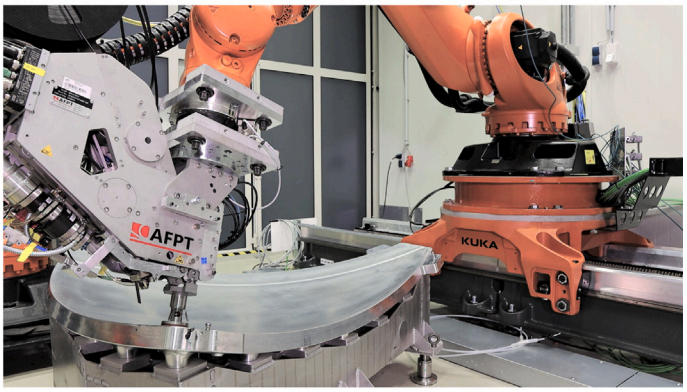

(d) 2nd COVER-generated engagement pose

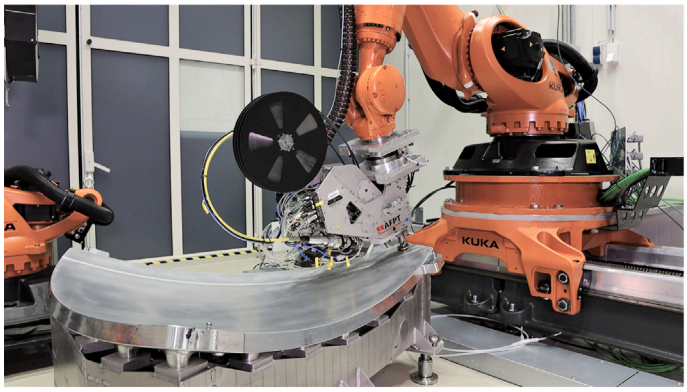

(e) 3rd COVER-generated engagement pose

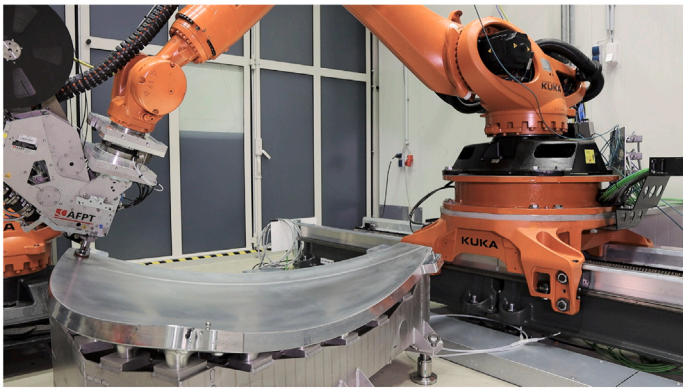

(f) 4th COVER-generated engagement pose

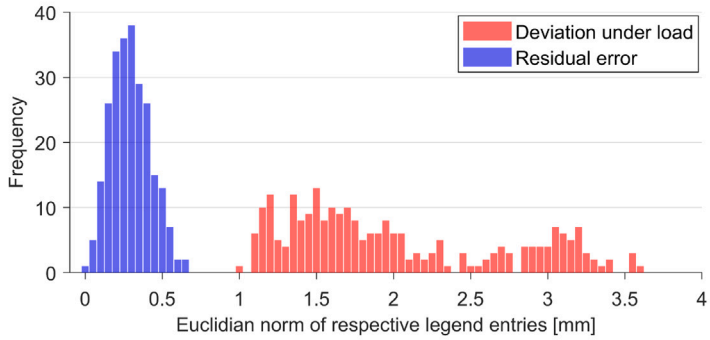

(g) Distribution of the norms of all commanded TCP displacements during the IREC calibration (red) and norms of least-square residual errors (blue) after solving the kinetostatic observation system using Eq.(19)

Fig. 8. Illustration of the minimally-invasive in-situ deployment of the IREC calibration tool and method for the elastic calibration of a T-AFP robotic workcell. The calibration poses correspond to the 31 COVER-generated poses appearing as cyan circles in Fig. 3. The load cases have been defined with $f_x = f_y = 280\ N$ and $f_z = 1100\ N$ to cover the maximal amplitudes of the process forces expected during T-AFP production while remaining within the allowable maximum continuous torques of the KUKA KR 120 HA industrial robot.

further accredited the choice of the k-vertex Gon COVER heuristics as our method of choice for industrial deployments of the IREC method. The Codecs in Fig. 7 also provided a very meaningful diagnostics tool to find out when the accuracy growth would have sufficiently stabilized during the calibration process, corroborating our initial choice of $N = 31$ poses.

Interestingly, this finding questions the need to consider an observability index as the main metrics for the segregation between candidate poses during a pose search algorithm used to generate a minimal set of poses for calibration. In particular, the Codecs in Fig. 7 suggest that, while new poses are being added iteratively, the fastest improvement in the robot mean and maximum accuracy during the IREC calibration might not be entirely correlated with a maximized O_1 index. The use of a metric criterion that expresses a degree of spatial coherence between the distribution of the poses and the spectrum of action of the robot in production, such as what we have attempted with the COVER heuristics, appears to have, for a same number of poses, a greater influence on the growth of the accuracy during the calibration process, at least as it pertains to the data recorded during the IREC method. It would certainly be insightful to exploit the CODEC algorithm in order to further investigate the degree of correlation between the growth of the mean and maximum accuracy during the calibration process with the evolution of other indices constructed mathematically using the entries of the matrix observation system.

4.2.4. Effect of the elastic model on the growth of accuracy

At the early stages of our research in the field of elastic robot calibration, we started by exploiting a kinetostatic model with $n_a = 6$ elasticities lumped about the axes of the motorized joints of the robot [65]. We progressively increased the complexity of the model until we established the aforementioned 18-DOF kinetostatic model as our standard. For the benefit of the reader, and in order to illustrate this evolution, we have generated the Codecs obtained by formulating and later solving Eq. (19) using each of these two models. The resulting Codecs are displayed in Fig. 9. The highlighted weaker convergence of the 6-DOF kinetostatic model can be interpreted by its lower ability, compared to the 18-DOF model, to capture the full complexity of the signatures in the robot non-axial deformation physics during the IREC calibration. The benefits of exploiting a 18-DOF kinetostatic model for elastic calibration appear significant.

4.2.5. Effect of load cases on the growth of accuracy

The last pillar of the IREC elastic calibration method, i.e., the architecture of the load cases, is finally investigated in this subsection. As an example of the insight that can be obtained in this case as well, we exploited the CODEC algorithm to compare two scenarios where the train sets are constructed using load cases that are either 1. purely normal to the surface $\mathcal{S}$ or 2. exploiting the five multidirectional load cases ${}^{\ell}\mathbf{f}_j$, $\ell = 1$ to 5, defined in Section 4.1. The resulting Codecs are displayed in Fig. 10. These results show the significant value of exploiting more elaborate multidirectional load cases in conjunction with the IREC method.

4.2.6. Accuracy improvement during AFP processing

Following its implementation in the real-time architecture shown in Fig. 5, the calibrated 18-DOF kinetostatic model has been successfully exploited to correct robot deviations during T-AFP additive manufacturing of a 3D thermoplastic section of a rear pressure dome (one of the 8 sections of a dome whose design is investigated for future generation commercial aircrafts), as shown in Fig. 11(a–h).

In particular, important precision improvements have been obtained in the measured side deviation throughout the produced part following activation of the real-time model-based compensation (see Table 1 for details). This accuracy performance obtained during deposition of laminates was shown to meet our ±0.3 mm targeted tolerance for the maximum allowed elastic side deviation of the robot TCP during production trajectories of the T-AFP workcell.

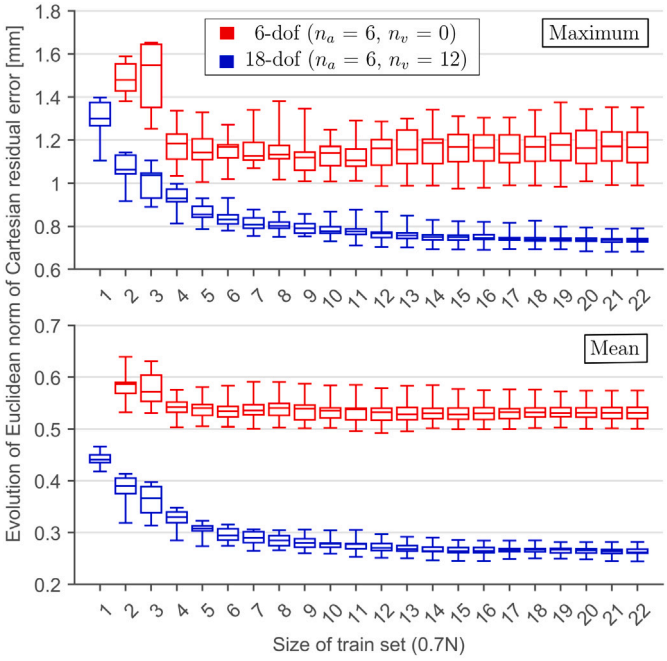

Fig. 9. Accuracy competency development charts constructed using the CODEC algorithm with the dataset obtained during IREC calibration of the T-AFP robotic test-bed with $N = 31$ poses. The two charts illustrate the growth of the mean and maximum robot accuracy as a function of the number of poses in the case of the exploitation of a kinetostatic model with either 6 (red) or 18 (blue) degrees of freedom.

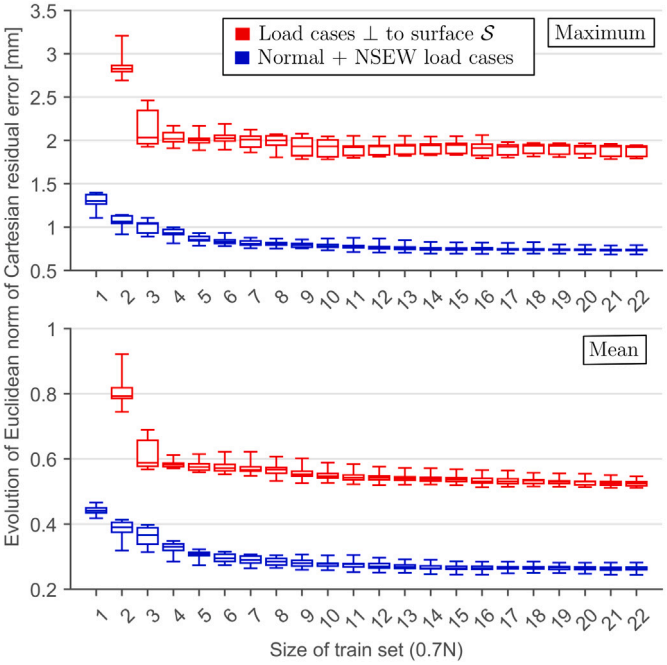

Fig. 10. Accuracy competency development charts constructed using the CODEC algorithm on the dataset obtained during IREC calibration of the T-AFP robotic test-bed with $N = 31$ poses. The two charts illustrate the growth of the mean and maximum robot accuracy as a function of the number of poses in the case of the construction of the train set using load cases that are either purely normal to the surface $\mathcal{S}$ (red) or exploiting the five multidirectional load cases ${}^{\ell}\mathbf{f}_j$, $\ell = 1$ to 5, presented in Section 4.1 (blue). In both cases, the same combinations of COVER-generated validation sets of $0.3N$ poses, exploiting the five multidirectional load cases ${}^{\ell}\mathbf{f}_j$, $\ell = 1$ to 5, were used to represent the targeted spectrum of action of the robot in production.

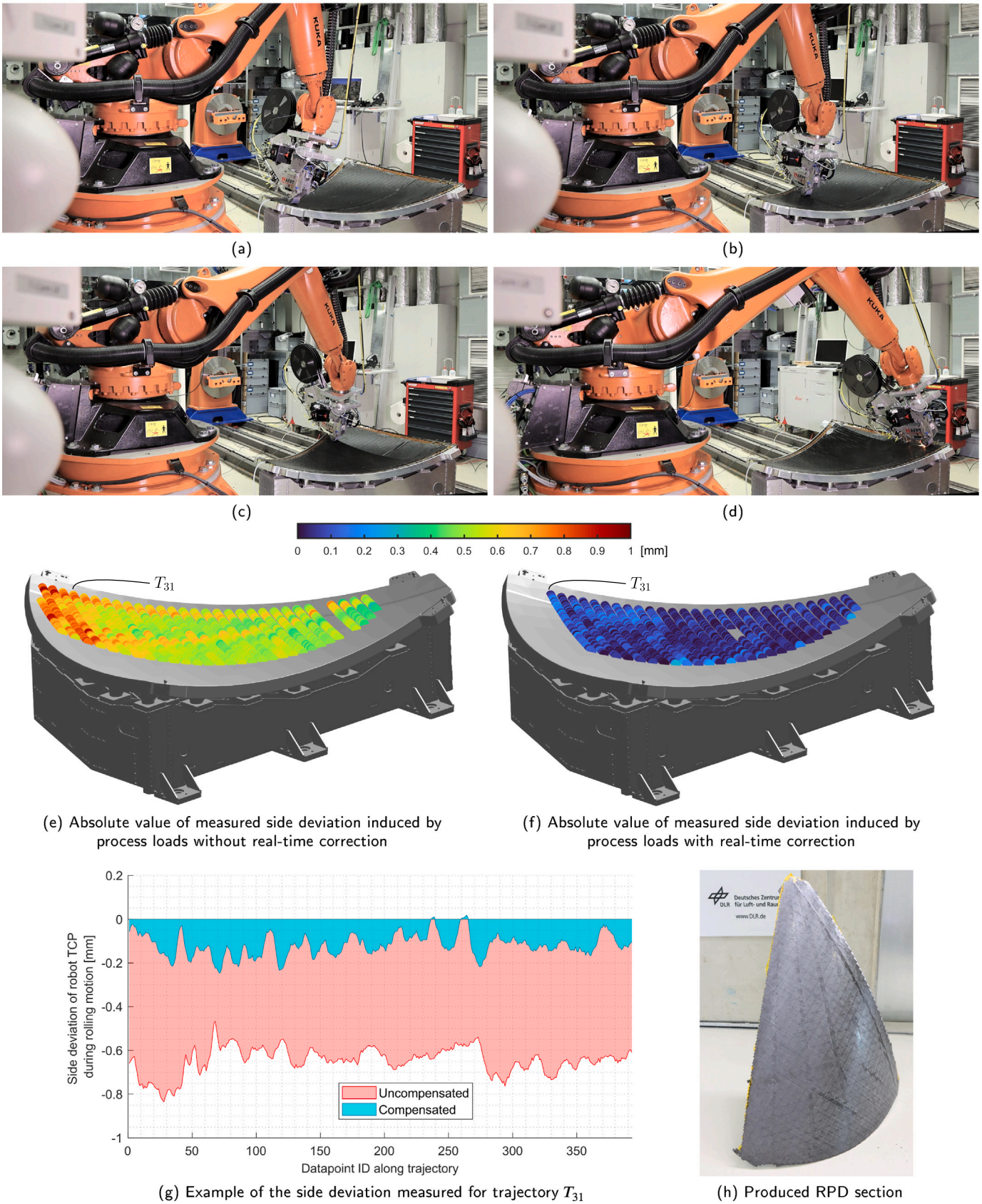

Fig. 11. Robotized T-AFP additive manufacturing of a 3D thermoplastic section of a representative commercial aircraft rear pressure dome (RPD), where process induced deviations are compensated in real-time using the IREC-calibrated 18-DOF kinetostatic model. (a–d) Illustration of the T-AFP manufacturing of ply #7 of 10, during which a Leica T-Mac 6D tracking device [66] mounted on the AFPT end-effector is used to record the robot motion at a frequency of 100 Hz for performance evaluation. (e,f) Measured side deviation induced by T-AFP process loads without/with activation of the real-time path correction.(g) Process-induced side deviation measured for trajectory T_{31}. (h) One of the RPD sections produced with real-time correction.

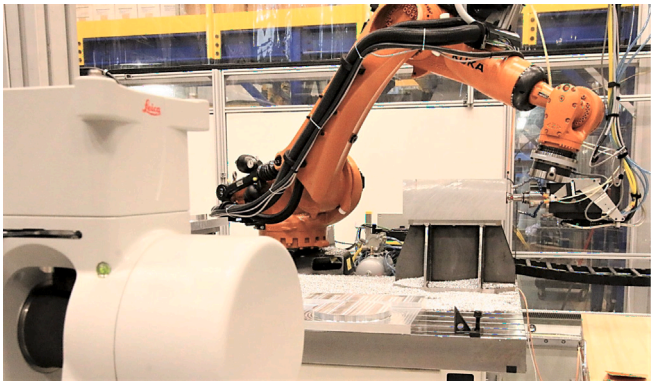

(a) Illustration of one of the tribologically-resisted engagements, during an IREC procedure, between the calibration tool (mounted in the spindle's HSK 63A adaptor) and one of the faces of the parallelepiped-shaped block of rough material before material removal.

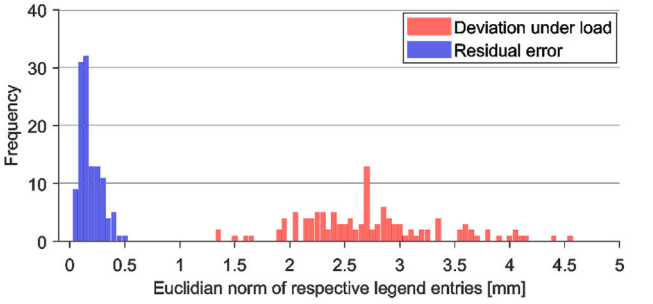

(b) Distribution of the norms of all commanded TCP displacements during the IREC calibration (red) and norms of least-square residual errors (blue) after solving the kinetostatic observation system using Eq.(19) for 15 engagement poses.

Fig. 12. Illustration of the in-situ deployment of the IREC calibration tool and method for the elastic calibration of a robotized machining workcell. The load cases have been defined with $f_x = f_y = 500\ N$ and $f_z = 1500\ N$ to cover the maximal amplitudes of the process forces expected during robotized machining operations while remaining within the allowable maximum continuous torques of the KUKA KR 300 Quantec Ultra industrial robot.

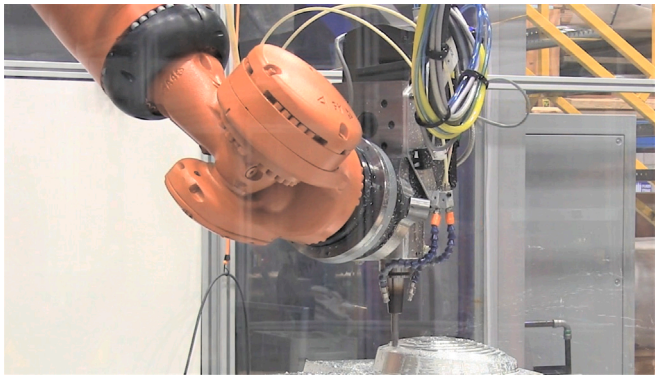

(a) Robotized machining of an Al-7075 aerospace part

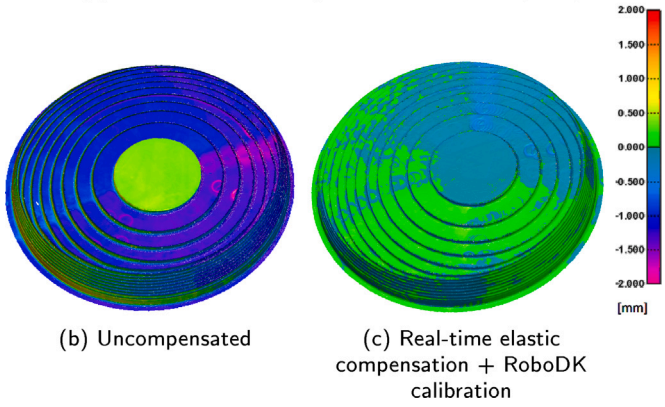

(b) Uncompensated (c) Real-time elastic compensation + RoboDK calibration

Fig. 13. Robotized roughing of an Al-7075 aerospace part (spindle speed: 12 000 RPM, feed rate: 70 mm/s) where process induced deviations are compensated in real-time using the IREC-calibrated 18-DOF kinetostatic model. (a) Illustration of the robotized roughing of a dome-shaped feature. After termination of the roughing phase, the dome was scanned using a FARO Edge ScanArm [67] and the cloud of point was compared in Polyworks Inspector [68] with the simulated nominal condition of the part. The resulting error map were produced (b) without and (c) with model-based path correction. (*Notes:* The top central disk was not machined in this roughing phase, thus explaining the very high accuracy in that central area in subfigures (b) and (c). The lower portion of the part is hidden in subfigure (a) to maintain confidentiality.)

4.3. Case study #2: Robotized machining of an aluminium aerospace part

4.3.1. Robotized machining testbed

In this second aerospace manufacturing case study, the robotized machining of a Al-7075 aerospace part is performed on a KUKA KR 300 Quantec Ultra robot. The robot mounted machining system, as shown in Fig. 13(a), comprises a spindle (18 kW capacity, 15 Nm @ 12000 RPM) and minimum quantity lubrication (MQL) external dual nozzle system. The objective of maximizing the productivity of the system is achieved mainly by maximizing the machining feedrate, which results in higher cutting forces. This, in turn, generates greater robot deviations which increases the requirement for an efficient path correction to ensure that the part can be produced within tight aerospace tolerances.

Another important aspect in this particular case study is that discretized robot postures were considered for optimization to offer the highest elastostatic Cartesian stiffness and dynamic responses. While dynamic responses were analyzed through FRF modal testing using impact hammer tests, elastostatic stiffness optimization exploited the same 18-DOF kinetostatic model calibrated using the IREC method as the one implemented for real-time path compensation.

4.3.2. IREC calibration of robotized machining testbed

In-situ elastic calibration of the robotized machining workcell was performed through application of the IREC apparatus and method as illustrated in Fig. 12(a). In this embodiment of the IREC procedure, the constraint used for the elastic calibration was the parallelepiped-shaped block of rough material before material removal. The block of rough material spans precisely the volume of the robot's workspace where accuracy is needed during machining operations. A set of 15 poses were used throughout all of the block's faces in combination with two laser tracker stations to ensure the visibility of the metrology marker during the calibration sequence. The output of the IREC calibration is shown in Fig. 12(b). These results confirm the relevance of the use of the 18-DOF kinetostatic model in conjunction with this embodiment of the IREC method for deployment in industrial robotized machining workcells.

4.3.3. Accuracy improvement during robotized machining

Following its implementation in the real-time architecture shown in Fig. 5, the calibrated 18-DOF kinetostatic model has been exploited to correct robot deviations during robotized roughing of an Al-7075 aerospace part, as shown in Fig. 13(a–c).

Important improvements have been obtained in the part accuracy after the roughing phase following activation of the real-time model-based compensation (see Table 1 for details). The dome feature could be machined within an error window very close to ±0.5 mm, which was our targeted tolerance for the roughing of this family of aerospace parts.

5. Analysis of the case studies' results and generalizability of the methodology

The results that have been obtained in terms of improvement of robot accuracy under process loads in the context of the two industry-grade aerospace case studies are summarized in Table 1. The mean TCP deviations have been reduced by 89.30% for robotized AFP and 83.08% for robotized roughing, respectively. The maximum TCP deviations have been reduced by 70.19% and 74.63%, respectively. In both cases, as it can be seen in Figs. 11(f,g) and 13(c), the distribution of the residual errors is very homogeneous throughout the geometries of the produced parts. Some light residual errors remain, such as light fluctuations in Fig. 11(f,g) as well as light tool marks in Fig. 13(c), that might be attributable to gear train backlash, dynamic oscillations and/or servo control phenomena. These residual errors have been reduced to amplitudes small enough that our process tolerances could be met in both case studies. It is noteworthy that, in the event of tighter process tolerances, it would be possible to adapt the presented innovations on robots equipped with secondary encoders, an approach that we are planning to explore in a follow-up phase of this research.

These results in Table 1 compare advantageously to the most recent literature in the field of model-based robot path correction under load where the reported reduction of the mean robot deformation is within a window ranging from 65% to 90% in the case of trajectories at velocities up to 50 mm/s [27]. Another recently-published work in this field reports a reduction of the maximum absolute error of 78.12% in a robotized machining scenario using a path correction scheme involving a domain-adversarial neural network [20].

Most importantly, beyond the quality of the results summarized in Table 1, and in echo to the schematic illustration of the prior art in Fig. 1, what differentiates the innovations brought by the present work is that the elastic model could be calibrated with multidirectional forces over a large workspace with a minimally-invasive technology. The latter can be efficiently deployed in production settings for large-scale manufacturing applications, thus offering a high potential for adoption by the aerospace industry and beyond.

As many manufacturing processes involve contact operations between a robot and parts supported by toolings and/or fixtures, the IREC procedure, complemented by the presented COVER and CODEC algorithms, offers a great potential for deployments in a variety of other contact processes where accuracy is required, such as incremental sheet forming, Friction Stir Welding (FSW), ultrasonic welding, drilling/fastening, and several others.

6. Conclusion and future work

In this paper, we have presented a novel in-situ elastic robot calibration (IREC) apparatus and method that has been formulated to conciliate requirements of minimal invasiveness, for seamless deployment in industrial settings, together with a high degree of coherence of the calibration protocol with the spectrum of action of the robot in production. This high degree of coherence is made possible in the IREC method thanks to the generation of tribologically-resisted load cases against production toolings, emblematic of the loci of process execution, in a reduced, but well-distributed, set of calibration poses thank to the use of a metric k-vertex Gon cover heuristics (COVER). The calibration apparatus and method are presented through the lens of accuracy competency development charts (Codecs), the graphical outputs of a repeated cross-validation algorithm that allows visualizing how the accuracy of deviation under load prediction grows during the calibration as a function of number and distribution of calibration poses, and how it is influenced by the nature of load cases and the complexity of the elastic model.

Two case studies are presented that illustrate different embodiments of the IREC method. In the first case study, a robotized T-AFP workcell is calibrated through load cases against the double curvature mold used for additively depositing thermoplastic prepreg tapes. In the second case study, a robotized machining unit is calibrated through load cases against the parallelepiped-shaped block of rough material before material removal. In both cases, the calibrated 18-DOF elastic model has been successfully implemented in a Linux Xenomai real-time target in order to compensate deviations induced by process forces in real-time during T-AFP and machining of full size aerospace parts. Our targeted process tolerances are reached in both applications thanks to the implementation of the presented technology and algorithms.

Table 1
Summary of the accuracy improvements achieved in the context of the two presented aerospace case studies using the proposed IREC method and path correction approach.

	Mean	Max	St. Dev.
Robotized AFP processing of a 3D thermoplastic aerostructure			
Absolute value of lateral deviation without correction (mm)	0.570	0.956	0,100
With proposed correction method (mm)	0.061	0.285	0,046
Reduction	89.30 %	70.19 %	54.00 %
Robotized roughing of an Al-7075 aerospace part			
Absolute value of on-part error with no correction (mm)	0,597	2,050	0,725
With proposed correction method (mm)	0,101	0,520	0,342
Reduction	83,08 %	74,63 %	52,83 %

The authors are pursuing research activities in direct continuation of the work presented in this paper, including:

- The adaptation of the presented innovations to robotic platforms equipped with secondary encoders.
- Self-calibration embodiments of the IREC apparatus and method allowing the achievement of comparable accuracy performance without the use of metrology.
- The advancement of accuracy management and control technologies in aerospace manufacturing platforms using cooperating robots.

CRediT authorship contribution statement

Bruno Monsarrat: Conceptualization, Funding acquisition, Methodology, Software, Investigation, Project administration, Supervision, Writing – original draft, Writing – review & editing. **Julien-Mathieu Audet:** Conceptualization, Methodology, Software, Investigation, Writing – original draft, Writing – review & editing. **Yves Fortin:** Conceptualization, Methodology, Software, Investigation. **Gabriel Côté:** Methodology, Software, Investigation, Writing – original draft. **Michael Vistein:** Methodology, Software, Investigation. **Lars Brandt:** Methodology, Project administration, Supervision, Investigation, Writing – original draft. **Ahmad Sadek:** Methodology, Software, Investigation, Supervision, Writing – original draft. **Florian Krebs:** Funding acquisition, Project administration, Supervision.

Declaration of competing interest

The authors declare the following financial interests/personal relationships which may be considered as potential competing interests: Bruno Monsarrat has patent #WO2016151360 - MULTI-JOINTED ROBOT DEVIATION UNDER LOAD DETERMINATION issued to NATIONAL RESEARCH COUNCIL OF CANADA. Yves Fortin has patent

#WO2016151360 - MULTI-JOINTED ROBOT DEVIATION UNDER LOAD DETERMINATION issued to NATIONAL RESEARCH COUNCIL OF CANADA.

Data availability

Data will be made available on request.

Acknowledgments

The authors wish to acknowledge the financial support of the National Program Office (NPO) of the National Research Council Canada (NRC). The authors are grateful to M. Darcy Burgess, and the whole team from NRC's Design and Fabrication Services (DFS), for designing and fabricating the double curvature T-AFP mold used in this research. The authors would also like to thank the technical teams at both NRC-AMTC and DLR-ZLP for their remarkable work during the experimental phases of this research.

Appendix A. Supplementary data

Supplementary material related to this article can be found online at https://doi.org/10.1016/j.rcim.2024.102743.

References

[1] Aerospace Robotics Market - Global Forecast to 2026, Report AS 4847, MarketsAndMarkets, 2021, URL https://www.marketsandmarkets.com/Market-Reports/aerospace-robotic-market-164758944.html.
[2] R. Bogue, The growing use of robots by the aerospace industry, Ind. Robot 45 (6) (2020) 705–709.
[3] R. DeVieg, Expanding the use of robotics in airframe assembly via accurate robot technology, SAE Int. J. Aerosp. 3 (1) (2010) 198–203.
[4] Y.M. Zhao, Y. Lin, F. Xi, S. Guo, Calibration-based iterative learning control for path tracking of industrial robots, IEEE Trans. Ind. Electron. 62 (5) (2015) 2921–2929.
[5] A. Frommknecht, J. Kuehnle, I. Effenberger, S. Pidan, Multi-sensor measurement system for robotic drilling, Robot. Comput.-Integr. Manuf. 47 (2017) 4–10.
[6] P. Prat, J. Malvaut, F. Villegoureix, Method for positioning an assembly tool at the end of an articulated arm and device for implementing the same, 2007, WO/2007/090981 patent.
[7] P. Prat, E. Gueydon, Cooperative robots for full automation, in: Procceedings of the SAE Aerospace Manufacturing Technology Conference and Exposition, Paper No. 2011-01-2536, 2011.
[8] E. Abele, J. Bauer, M. Pischan, O. von Stryk, M. Friedmann, T. Hemker, Prediction of the tool displacement for robot milling applications using coupled models of an industrial robot and removal simulation, in: Proceedings of the CIRP 2nd International Conference on Process Machine Interactions, 2010.
[9] C. Reinl, M. Friedmann, J. Bauer, M. Pischan, E. Abele, O. von Stryk, Model-based off-line compensation of path deviation for industrial robots in milling applications, in: Procceedings of the IEEE/ASME International Conference on Advanced Intelligent Mechatronics, AIM, 2011, pp. 367–372.
[10] J. Cortsen, H.G. Petersen, Advanced off-line simulation framework with deformation compensation for high speed machining with robot manipulators, in: Procceedings of the IEEE/ASME International Conference on Advanced Intelligent Mechatronics, AIM, 2012, pp. 934–939.
[11] J. Belchior, M. Guillo, E. Courteille, P. Maurine, L. Leotoing, D. Guines, Off-line compensation of the tool path deviations on robotic machining: Application to incremental sheet forming, Robot. Comput.-Integr. Manuf. 29 (2013) 58–69.
[12] S. Marie, E. Courteille, P. Maurine, Elasto-geometrical modeling and calibration of robot manipulators: Application to machining and forming applications, Mech. Mach. Theory 69 (2013) 13–43.
[13] A. Klimchik, A. Pashkevich, D. Chablat, G. Hovland, Compliance error compensation technique for parallel robots composed of non-perfect serial chains, Robot. Comput.-Integr. Manuf. 29 (2013) 385–393.
[14] M. Haage, M. Halbauer, C. Lehmann, J.P. Staedter, Increasing robotic machining accuracy using offline compensation based on joint-motion simulation, in: Proceedings of the 41st International Symposium on Robotics, ISR/Robotik, 2014, pp. 1–8.
[15] N.R. Slavkovic, D.S. Milutinovic, M.M. Glavonjic, A method for off-line compensation of cutting force-induced errors in robotic machining by tool path modification, Int. J. Adv. Manuf. Technol. 70 (2014) 2083–2096.
[16] M. Cordes, W. Hintze, Offline simulation of path deviation due to joint compliance and hysteresis for robot machining, Int. J. Adv. Manuf. Technol. 90 (2017) 1075–1083.
[17] K. Kolegain, F. Leonard, S. Zimmer-Chevret, A. Ben Attar, G. Abba, A feedforward deflection compensation scheme coupled with an offline path planning for robotic friction stir welding, in: Proceedings of the IFAC Conference, Vol. 51, 2018, pp. 728–733, (11).
[18] K. Kolegain, F. Leonard, S. Chevret, A. Ben Attar, G. Abba, Off-line path programming for three-dimensional robotic friction stir welding based on Bézier curves, Ind. Robot 45 (5) (2018) 669–678.
[19] F. Schnoes, M.F. Zaeh, Model-based planning of machining operations for industrial robots, in: Proceedings of the 17th CIRP Confernce on Modelling of Machining Operations, Vol. 82, 2019, pp. 497–502.
[20] C. Ye, J. Yang, H. Ding, High-accuracy prediction and compensation of industrial robot stiffness deformation, Int. J. Mech. Sci. 233 (2022) 107638.
[21] H. Zhang, J. Wang, G. Zhang, Z. Gan, Z. Pan, H. Cui, Z. Zhu, Machining with flexible manipulator: toward improving robotic machining performance, in: Proceedings of the IEEE/ASME International Conference on Advanced Intelligent Mechatronics, 2005, pp. 1127–1132.
[22] Z. Pan, H. Zhang, Robotic machining from programming to process control: a complete solution by force control, Ind. Robot 35 (5) (2008) 400–409.
[23] J. Wang, H. Zhang, T. Fuhlbrigge, Improving machining accuracy with robot deformation compensation, in: Procceedings of the IEEE/RSJ International Conference on Intelligent Robots and Systems, 2009, pp. 3826–3831.
[24] Z. Pan, H. Zhang, Improving robotic machining accuracy by real-time compensation, in: Proceedings of the IEEE ICCAS-SICE International Joint Conference, 2009, pp. 4289–4294.
[25] U. Schneider, M. Momeni-K, M. Ansaloni, A. Verl, Stiffness modeling of industrial robots for deformation compensation in machining, in: Proceedings of the IEEE/RSJ International Conference on Intelligent Robots and Systems, 2014, pp. 4464–4469.
[26] M. Guillo, L. Dubourg, Impact and improvement of tool deviation in friction stir welding: Weld quality and real-time compensation on an industrial robot, Robot. Comput.-Integr. Manuf. 39 (2016) 22–31.
[27] M.K. Gonzalez, N.A. Theissen, A. Barrios, A. Archenti, Online compliance error compensation system for industrial manipulators in contact applications, Robot. Comput.-Integr. Manuf. 76 (2022) 102305.
[28] M.F. Zaeh, F. Schnoes, B. Obst, D. Hartmann, Combined offline simulation and online adaptation approach for the accuracy improvement of milling robots, CIRP Ann. 69 (1) (2020) 337–340.
[29] A. Jubien, M. Gautier, Global identification of spring balancer, dynamic parameters and drive gains of heavy industrial robots, in: Proceedings of the IEEE/RSJ International Conference on Intelligent Robots and Systems, IROS, 2013, pp. 1355–1360.
[30] K. Yang, W. Yang, G. Cheng, B. Lu, A new methodology for joint stiffness identification of heavy duty industrial robots with the counterbalancing system, Robot. Comput.-Integr. Manuf. 53 (2018) 58–71.
[31] J. Tenhumberg, B. Bäuml, Calibration of an elastic humanoid upper body and efficient compensation for motion planning, in: Proceedings of the IEEE-RAS 20th International Conference on Humanoid Robots, Humanoids, 2020, pp. 98–103.
[32] Y. Song, M. Liu, B. Lian, Y. Qi, Y. Wang, J. Wu, Q. Li, Industrial serial robot calibration considering geometric and deformation errors, Robot. Comput.-Integr. Manuf. 76 (2022) 102328.
[33] K. Deng, D. Gao, S. Ma, C. Zhao, Y. Lu, Elasto-geometrical error and gravity model calibration of an industrial robot using the same optimized configuration set, Robot. Comput.-Integr. Manuf. 83 (2023) 102558.
[34] A. Klimchik, S. Caro, A. Pashkevich, Practical identifiability of the manipulator link stiffness parameters, in: ASME International Mechanical Engineering Congress and Exposition, 2013, pp. 1–10.
[35] A. Klimchik, Y. Wu, S. Caro, B. Furet, A. Pashkevich, Geometric and elastostatic calibration of robotic manipulator using partial pose measurements, Adv. Robot. 28 (2014) 1419–1429.
[36] A. Klimchik, B. Furet, S. Caro, A. Pashkevich, Identification of the manipulator stiffness model parameters in industrial environment, Mech. Mach. Theory 90 (2015) 1–22.
[37] S. Kolyubin, A. Shiriaev, A. Jubien, Consistent kinematics and dynamics calibration of lightweight redundant industrial manipulators, Int. J. Adv. Manuf. Technol. 101 (2019) 243–259.
[38] C. Icli, O. Stepanenko, I. Bonev, New method and portable measurement device for the calibration of industrial robots, Sensors 20 (2020) 5919.
[39] R.A. Boby, Identification of elasto-static parameters of an industrial robot using monocular camera, Robot. Comput.-Integr. Manuf. 74 (2022) 102276.
[40] G. Alici, B. Shirinzadeh, Enhanced stiffness modeling, identification and characterization for robot manipulators, IEEE Trans. Robot. 21 (4) (2005) 554–564.
[41] C. Dumas, S. Caro, M. Chérif, S. Garnier, A methodology for joint stiffness identification of serial robots, in: Proceedings of the IEEE/RSJ International Conference on Intelligent Robots and Systems, 2010.
[42] N.R. Slavkovic, D.S. Milutinovic, B.M. Kokotovic, M.M. Glavonjic, S.T. Zivanovic, K.F. Ehmann, Cartesian compliance identification and analysis of an articulated machining robot, FME Trans. 41 (2013) 83–95.
[43] N.A. Theissen, T. Laspas, A. Archenti, Closed-force-loop elastostatic calibration of serial articulated robots, Robot. Comput.-Integr. Manuf. 57 (2019) 86–91.

[44] C. Lehmann, B. Olofsson, K. Nilsson, M. Haage, A. Robertsson, O. Sörnmo, U. Berger, Robot joint modeling and parameter identification using the clamping method, in: Proceedings of the IFAC Conference on Manufacturing Modelling, Management and Control, MIM, 2013.
[45] A. Jubien, G. Abba, M. Gautier, Joint stiffness identification of a heavy Kuka robot with a low-cost clamped end-effector procedure, in: 2014 11th International Conference on Informatics in Control, Automation and Robotics, ICINCO, Vol. 02, 2014, pp. 585–591.
[46] K. Nilsson, Method and system for determination of at least one property of a joint, 2014, WO/2014/065744 patent.
[47] K. Kamali, A. Joubair, I.A. Bonev, P. Bigras, Elasto-geometrical calibration of an industrial robot under multidirectional external loads using a laser tracker, in: Procceedings of the IEEE International Conference on Robotics and Automation, 2016, pp. 4320–4327.
[48] K. Kamali, I.A. Bonev, Optimal experiment design for elasto-geometrical calibration of industrial robots, IEEE/ASME Trans. Mechatronics 24 (6) (2019) 2733–2744.
[49] Multidimensional arrays, 2023, https://www.mathworks.com/help/matlab/matrices-and-arrays.html. Accessed: 2023-08-31.
[50] B. Monsarrat, Y. Fortin, Multi-jointed robot deviation under load determination, 2016, WO/2016/151360 patent.
[51] D. Zhang, Kinetostatic Analysis and Optimization of Parallel and Hy- brid Architectures for Machine Tools (PhD. Thesis), Laval University, 1999.
[52] D. Zhang, C. Gosselin, Kinetostatic modeling of N-DOF parallel mechanisms with a passive constraining leg and prismatic actuators, ASME J. Mech. Des. 123 (3) (2000) 375–381.
[53] C. Gosselin, D. Zhang, Stiffness analysis of parallel mechanisms using a lumped model, Int. J. Robot. Autom. 17 (1) (2002) 17–27.
[54] E. Abele, S. Rothenbücher, M. Weigold, Cartesian compliance model for industrial robots using virtual joints, Prod. Eng. 2 (3) (2008) 339–343.
[55] J. Angeles, Fundamentals of Robotic Mechanical Systems : Theory, Methods, and Algorithms, Springer-Verlag, New-York Inc., 1997.
[56] Y. Sun, J.M. Hollerbach, Observability index selection for robot calibration, in: Proc. IEEE International Conference on Robotics and Automation, 2008, pp. 831–836.
[57] T.J. Mitchell, An algorithm for the construction of d-optimal experimental designs, Techometrics 16 (1974) 203–210.
[58] D. Daney, Y. Papegay, B. Madeline, Choosing measurement poses for robot calibration with the local convergence method and Tabu search, Int. J. Robot. Res. 24 (6) (2005) 501–518.
[59] A. Joubair, I.A. Bonev, Comparison of the efficiency of five observability indices for robot calibration, Mech. Mach. Theory 70 (2013) 254–265.
[60] J. Garcia-Diaz, R. Menchaca-Mendez, R. Menchaca-Mendez, S. Pomares Hernández, J.C. Pérez-Sansalvador, N. Lakouari, Approximation algorithms for the vertex K-center problem: Survey and experimental evaluation, IEEE Access 7 (2019) 109228–109245.
[61] T.F. Gonzalez, Clustering to minimize the maximum intercluster distance, Theor. Comput. Sci. 38 (1985) 293–306.
[62] lsqlin to solve constrained linear least-squares problems, 2023, https://www.mathworks.com/help/optim/ug/lsqlin.html. Accessed: 2023-08-31.
[63] RoboDK calibration module, 2023, https://robodk.com/robot-calibration. Accessed: 2023-08-31.
[64] L. Brandt, D. Deden, J. Harig, F. Fischer, M. Kupke, Thermocouple based process optimization for laser assisted automated fiber placement of CF/LM-PAEK, J. Compos. Mater. (2023) http://dx.doi.org/10.1177/00219983231199833.
[65] A. Bres, B. Monsarrat, L. Dubourg, L. Birglen, C. Perron, M. Jahazi, L. Baron, Simulation of friction stir welding using industrial robots, Ind. Robot 37 (1) (2010) 36–50.
[66] T-Mac - 6DoF tracking device for automated applications, 2023, https://hexagon.com/products/leica-t-mac. Accessed: 2023-08-31.
[67] FARO edge ScanArm, 2023, https://www.hts-3d.com/techSheets/FARO-edge-scanarm-tech-sheet.pdf. Accessed: 2023-08-31.
[68] PolyWorks inspector, 2023, https://www.innovmetric.com/products/polyworks-inspector. Accessed: 2023-08-31.